POLITECNICO
MILANO 1863

SCUOLA DI INGEGNERIA INDUSTRIALE
E DELL'INFORMAZIONE

Study on the mechanical anisotropy of soft tissues by optical elastography

Tesi di Laurea Magistrale in
Biomedical Engineering - Ingegneria Biomedica

Author: **Sibylle Grégoire**

Student ID: 10783888
Advisor: Prof. Amir Nahas
Co-advisors: Prof. Andrea Aliverti
Academic Year: 2021-22

Abstract

Viscoelatic properties of biological tissue are of great interest for diagnostic purpose. Elastography aims not only at quantifying the routine palpation examinations performed by the clinicians but at retrieving elasticity and viscosity of any type of tissues in the body. To do so the propagation of mechanical waves in the body is imaged and processed to extract local viscoelastic properties. From mechanical point of view biological tissue are often highly anisotropic and can be described as transversely anisotropic.
Since 2000's, a new method based on correlation of a diffuse field and called noise correlation allows to retrieve elasticity with slow imaging techniques even though Shannon criteria of sampling isn't fullfill. Until now noise correlation as be proven to succesfully retrieve local elasticity only in isotropic media. The topic of this work is to provide a measurement technique of elasticity in transversely isotropic tissues using noise correlation technique.
Simulation of mechanical waves field are realised in isotropic and anisotropic media. Different shapes of waves sources are implemented. Coupling between anisotropy of the media and the shape of the autocorrelation of waves sources is highlighted. An uncoupling solution is proposed based on the simulations. An experimental verification is realised on isotropic and anisotropic agarose phantoms. Mechanical waves sources are controlled by piezoelectric actuators. Laser speckle imaging is used to detect mechanical waves propagation in the phantoms.
Uncoupling solution is proven to work using Laser speckle imaging on agarose samples. Tensor of elasticity of anisotropic agarose samples are retrieve with good comparison with litteracy values.

Keywords: Optical elastography, Shear waves, Transverse anisotropy, Laser speckle imaging, Noise correlation

Abstract in lingua italiana

Le proprietà viscoelastiche dei tessuti biologici sono di grande interesse a scopo diagnostico. L'elastografia non mira solamente a quantificare gli esami di palpazione di routine eseguiti dai medici, ma anche a recuperare l'elasticità e la viscosità di qualsiasi tipo di tessuto nel corpo. A tal fine, la propagazione delle onde meccaniche nel corpo viene fotografata ed elaborata per estrarre le proprietà viscoelastiche locali. Dal punto di vista meccanico, i tessuti biologici sono spesso altamente anisotropi e possono essere descritti come isotropi trasversali.

A partire dagli anni 2000, un nuovo metodo basato sulla correlazione di un campo diffuso e chiamato correlazione del rumore permette di recuperare l'elasticità con tecniche di imaging lente, anche se i criteri di campionamento di Shannon non sono soddisfatti. Fino ad ora la correlazione del rumore si è dimostrata in grado di recuperare con successo l'elasticità locale solo in mezzi isotropi. Il tema di questo lavoro è fornire una tecnica di misurazione del tensore dell'elasticità nei tessuti trasversalmente anisotropi utilizzando la tecnica della correlazione del rumore. La simulazione del campo di onde meccaniche è realizzata in mezzi isotropi e anisotropi. Sono state implementate diverse forme di sorgenti d'onda. Viene evidenziato l'accoppiamento tra l'anisotropia del mezzo e la forma dell'autocorrelazione delle sorgenti d'onda. Sulla base delle simulazioni viene proposta una soluzione di disaccoppiamento. Viene realizzata una verifica sperimentale su fantocci di agarosio isotropi e anisotropi. Le sorgenti di onde meccaniche sono controllate da attuatori piezoelettrici. L'imaging speckle laser viene utilizzato per rilevare la propagazione delle onde meccaniche nei fantocci.

La soluzione di disaccoppiamento è stata dimostrata utilizzando l'imaging laser speckle su campioni di agarosio. Il tensore di elasticità dei campioni di agarosio anisotropo viene recuperato con un buon confronto con i valori in letteratura.

Parole chiave: Elastografia ottica, onde di taglio, isotropia trasversale, laser speckle imaging, correlazione del rumore

Contents

Introduction

In soft tissue, mainly two types of elastic waves are propagating. First the compression waves, called P in seismology, that propagates by longitudinal strain and that are used in ultrasound system. Second, the shear waves, called S in seismology, that propagates by transverse strain and that are used in elastography [51]. Elastography is the cartography of viscoelastic properties of matter.

During any palpation examination, for instance an breast screening for detection of tumors, the elasticity of palpation to which the practitioner is sensible is the shear elasticity of the tissue [24]. Retrieving shear waves speed in a biological tissue is a measure of its stiffness. Since 1980, researshers have been able to propagate shear waves in the biological tissue and follow them to retrieve elasticity properties [33]. It gaves two main applications today in clinical use: the fibroscan in 2003, gives a value of the elasticity of the liver and helps to diagnose cirhosis, the Aixplorer in 2008, is the first echograph to embedded an elasticity measure that is superimposed to the sonogram to help diagnosis.

Most of biological tissues (muscles, skin, brain...) are layered tissues, anisotropically structured. This anisotropy of structure induces a mechanical anisotropy leading to different elastic and viscous modulus according to the direction of the stimuli. Muscles were demonstrated to exhibit high mecanical anisotropy both by ultrasound [27, 37] and by MRI [44, 47] . Mechanical anisotropy properties were found on the kidney [26, 38], with ultrasound system elastography. Brain tissue mechanical anisotropy was demonstrated through MRI [9, 29] . Breast lesion anisotropy is also under study in stage of tumor detection [16, 36]. Skeletal muscle was proven to be a good indiator of muscles necrosis [46]. Brain's anisotropy properties link with neuropathology like edema, ischemia or aging are under study [9, 29]. Kidney anisotropy was detected as a confounding factor for linking kidney's elasticity with kidney's fibrosis [38] .

Muscles presents an axial symmetry in any plane of the fibers [49]. For this specific case,

elastic theory predicts two types of shear waves, propagating anisotropically in the tissues with different polarisations [57]. The anisotropic propagation of two types of shear waves, called slow and fast has been demonstrated in muscle [25]. One is polarised inside the fiber's plane, one is polarised in the plane perpendicular to fiber's plane. Each of this shear waves will present different velocities in the parralel or in the perpendicular direction of the fibers.

Most of study on the mechanical anisotropy of biological tissue were realised using ultrasound based system [16, 36, 37] or MRI [9, 29, 45]. In particular, very low number of study uses optical elastography [56]. Optical elastography refers to the use of optical system to image shear waves propagation in tissue and retrieve elasticity. Digital holography, Optical coherence tomography, Laser speckle imaging are sensible to displacements in tissues normally to the surface. Those techniques can be used for intrinsecally filtering out one type of shear waves, the shear waves polarised in the plane perpendicular to fiber's plane.

In particular LASER speckle imaging offers several advantages: resolution, real time measure, low post processing treatment and it's especially low cost and easy of use [16, 48]. Laser speckle imaging elastography has been demonstrated to successfully retrieve both elasticity and viscosity of biological tissues [16]. Laser speckle imaging elastography is easely integrated in multimodal systems [12, 20].

In 2D imaging, to probe the elasticity according to the sample position, straightfoward idea is to rotate the sample while sending an excitation in a fixe direction, or inversely fixe the sample and rotate the excitation [56]. Passive elastography [13], also called noise correlation [40] allows to retrieve shear waves velocity in all the direction in one acquisition. It's derived from seismology correlation's techniques to retrieve waves velocity from ambient seismic noise [55]. This method uses a diffuse field of waves obtain by multiple scattering of an impulsion. This method offers two main advantages: it's compatible with slow imaging technique [15], like Laser Speckle Imaging, and it's usable in vivo without any external wave sources [23].

Measuring the mechanical anisotropy of biological tissues using noise correlation technique by Laser Speckle Imaging elastography offers numerous advantages. To summerize it's usable in vivo to retrieve anisotropy factor and elasticity of the matter with good resolution and in real time with an impressively cheap and simple set-up. Implemented in an endoscope or used during open surgery this technique could provide a very accessible, low risk, real time elasticity measurement tool.

In this work, finite difference simulations of elastic waves are performed. A bias in the noise correlation method for anisotropy retrieval is highlited. A classification algorithm is proposed to detect the cases where the anisotropic elasticities can be retrieved or not. Experimental phantoms of mechanically anisotrope samples are studied by Laser Speckle Imaging. First results are presented. Anisotropy in samples is retrieve with good correspondance. Bias in the noise correlation method is highlited experimentally. Comparison with the proposed classifier is performed.

1 | Elastography and elastic waves, state of the art

1.1. Elastography

During a medical examination, it's common for the physician to touch the patient to feel the elasticity of the skin and detect abnormalities. One classic example of palpation examination is routine breast screening. This palpation examination is limited by its qualitative, physician dependent output. Elastography aims at providing a quantitative measurement of the elasticity of any types of biological tissue. It provides a tool to the physicist to quantify and map the elasticity of upper layers skin, organs, biopsies. It's important to stress out the quantitative aspect of elastography, making it a much stronger tool than soft tissue imaging like CT, echograph or MRI than can detect masses or abnormalities but not characterized them.
Furthermore, biological tissues have a wide range of elasticity (see figure 1.1), promising for elastography a future not only as additional information but also as imaging technique by itself.

This section describes the underlying physics, the current axes of development and main challenges of elastography.

1.1.1. Introduction to elastography

Even though records of palpation exam are found in ancient Egypt (3100 BC) [10], elastography was developped in the late 1980. It followed the rise of echography as a gold standard imaging technique. The groundmaking work of [32] in 1980 provide a first ultrasound based in-vivo tracking tissue movements method. With this method stiff lesion of the prostate were imaged. Following this work, strain elastography was develloped in the 1990. It's based on strain measurement after a compression of the tissue by ultrasound. It's now a mature technology offered by most of echograph compagnies[24]. Infact, with very little change to classical echograph, one can add an elasticity measurement to provide

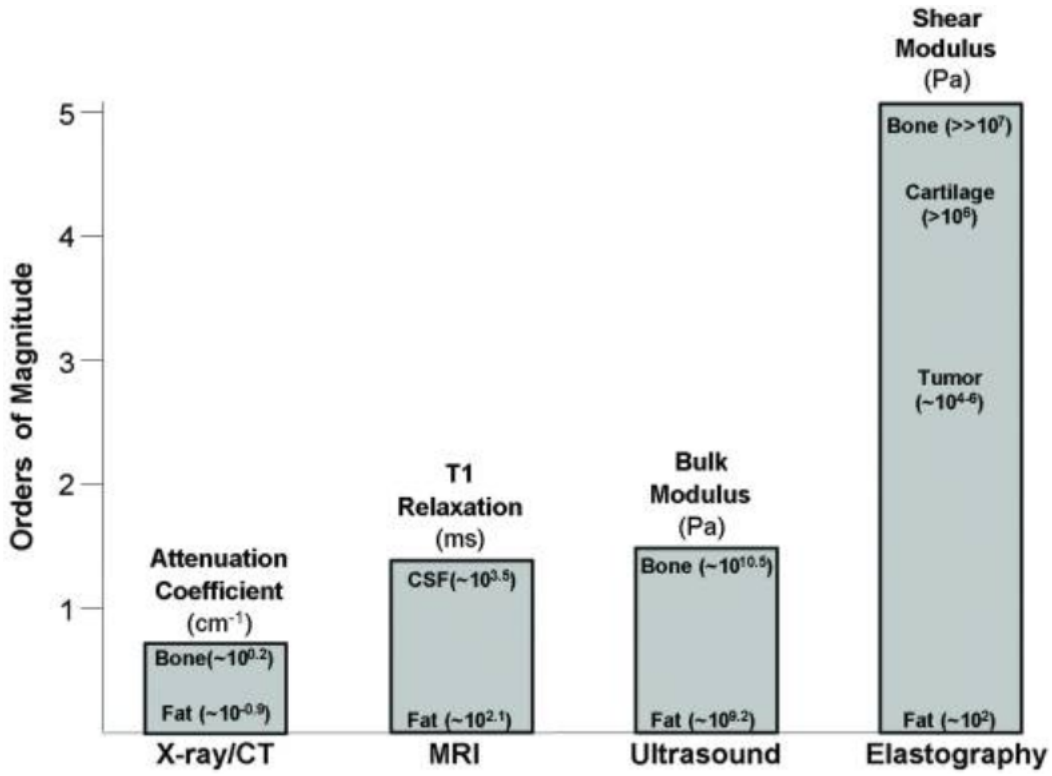

Figure 1.1: Imaging modality contrast mechanism [39]

on-line mapping of elasticity, as an usefull tool for image interpretation. One can see in figure 1.2 the use of an echograph on the diagnosis of breast lesion.

In the 2000s, the idea of following shear waves propagating in the tissue came up. In 2003, the first non-imaging device (Fibroscan, see figure 1.3) was introduced to diagnose fibrosis by providing a value of liver elasticity. Shear waves elastography only require to image the wave propagation. Therefore, it can by aplied with various types of imaging mainly MRI elastography and optical elastography.

1.1.2. The physics of elastography

Elastography is based on this general scheme:

- Create a mechanical perturbation in the tissue
- Measure the displacements in the tissue due to the perturbation
- Use a mechanical model to infer viscoelastic properties of the tissue from the measured displacements

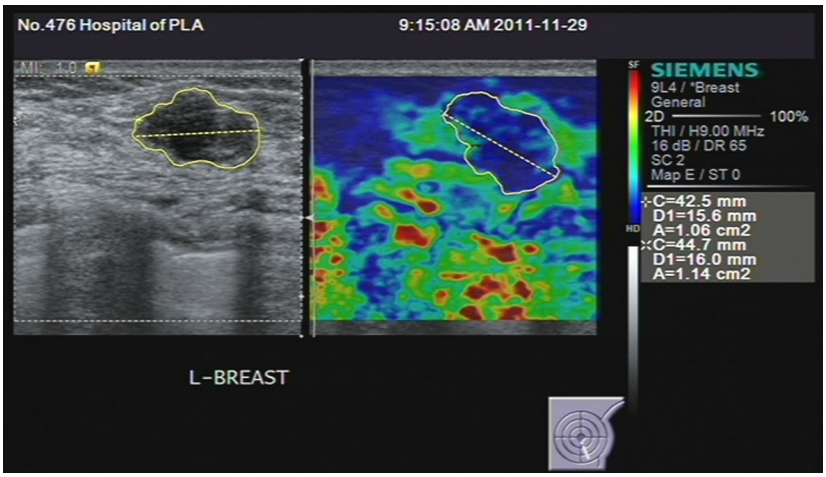

Figure 1.2: The left picture showing a B-mode ultrasonography locating the region of interest (ROI). The right picture showing the elastography of the breast lesion, with a blue colour indicating a harder tissue and a red colour indicated a softer tissue. [1]

Figure 1.3: Fibroscan [1]

The perturbation can first be static, for instance, a constant compression stress, and the measure displacement will be the resulting strain in the tissue. Or the perturbation can be transient, for instance a shear wave propagating in the tissue, and the measured displacement will be the deformation of the tissue due to waves propagation. Those two cases are refered to:

- static or quasistatic elasography also known as strain elastography
- transient or dynamic elastography

,

Quasistatic elastography

Quasistatic elastography is base on strain (ϵ) measurement after a static compression, a constant stress (σ) applied on the tissue (see figure 1.4).
Strain is defined as the deformation on distance to the compressor: $\epsilon = \frac{\delta L}{L}$ [19]. Stress and strain are linearly related by Hooke's law $\sigma = E\epsilon$, with E young modulus of the tissue. With a constant stress, strain in soft material is larger than in stiff one. To convince itself, the reader is invited to press his forearm muscle with or without contracting it.
Recording the displacements on a line perpendiculary to the compressor, one can draw strain elastogram (strain map). Figure 1.5 shows an elastogram of a breast carcinoma with comparison with a echograph's sonogram. The dark area show high stiffness, facilitating the diagnosis of a carcinoma.
Nevertheless, even if the strain elastogram are undoubtably link to stiffness, due to scatterer in the tissues, the stress is often unknown. With unknown stress it's difficult to be quantitative on elasticity modulus.

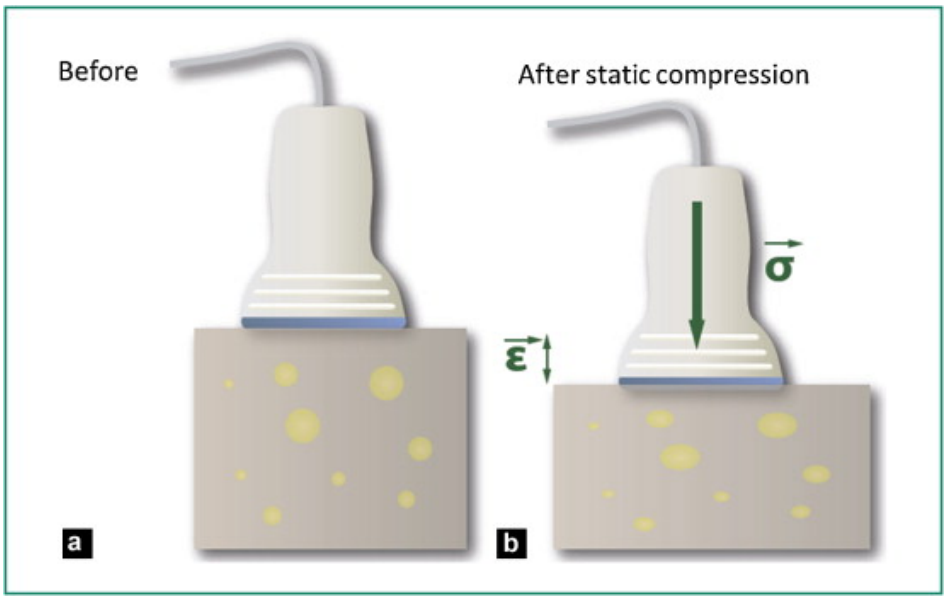

Figure 1.4: Quasistatic elastography principle [27]

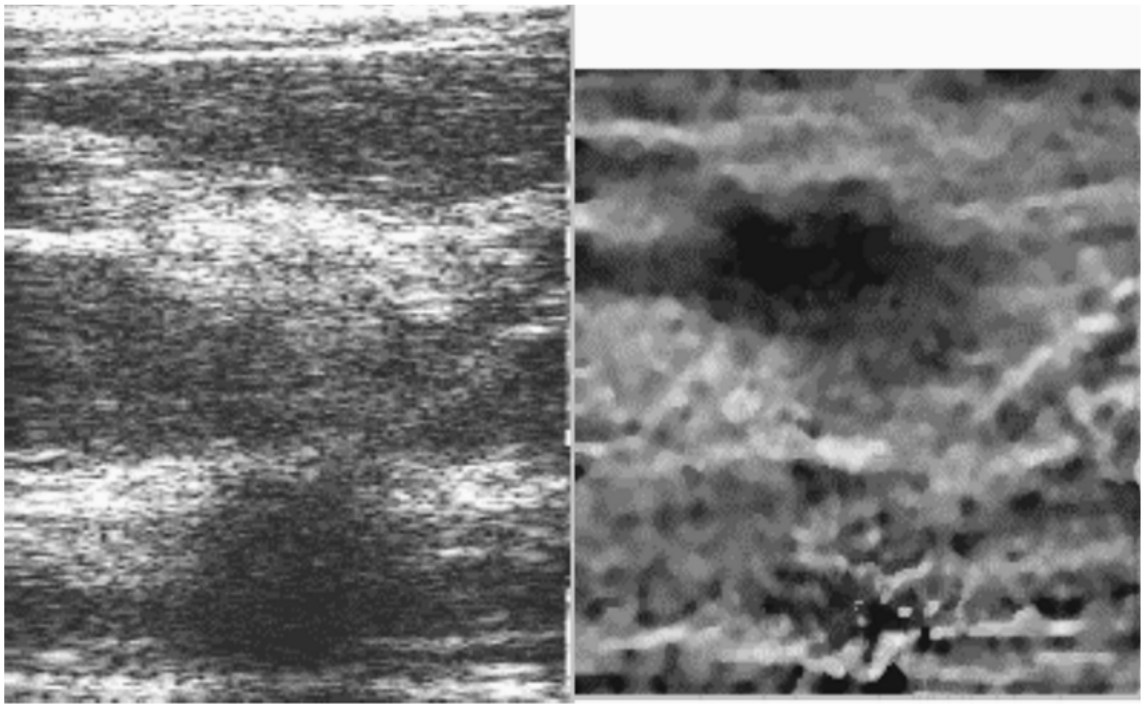

Figure 1.5: Sonogram (Left) and Strain elastogram (Right) of a breast carcinoma [24]

Transient elastography

Transient elastography recovers any techniques involving a dynamic stress. Most used and investigated dynamic stress is the one caused by the propagation of elastic waves.

Shear waves are elastic waves that propagate transversally in tissue. Elastic waves speed is an intrinsic characteristic of a media. In figure 1.6 the sound of the train propagates much faster in the rail than in the air.

Figure 1.6: Daltons listening to the train [5]

Mechanical waves propagate by local deformation of the media, the more the media is stiff, the highest will be his elastic modulus, the faster will be its deformation. Therefore, elastic waves travel faster in stiff media than in in soft one. Equation 1.1 is showing the straightfoward link between Young's modulus and shear waves speed, that holds in the case of incompressible, isotropic, homogeneous media (see section 1.2 for proper derivation).

$$E = 3\rho c^2_{shearwaves} \tag{1.1}$$

Under the assumption of an isotropic purely elastic solid, two main types of mechanical waves can propagate (see section 1.2 for proper derivation). The two types of waves propagated in tissue are compression waves, longitudinal waves traveling around 1500 m/s in soft tissues and shear waves, transverse waves traveling around 1-10 m/s in soft tissues. Shear waves are probing elastic properties of the matter and are used in elastography. Compression waves are linked to bulk properties and are used in echographs.

Numerous methods exist to induce shear waves in tissue. Main ones are acoustic radi-

ation force impulse excitation (ARFI) and controlled external vibration. ARFI induces shear waves but pushing locally on the tissue using acoustic pressure with an ultrasound probe. Controlled external vibration can induce shear waves by mechanical impulses with vibrators like piezoelectrics materials for instance.

Once shear waves are propagating in the tissue, numerous methods exists to image their propagation. Main imaging technique under research are:

- Ultrafast ultrasound elastography. Main benefits of the technique are to be online, 2D or 3D, easely coupled to ultrasound system.
- MRI elastography, that have the benefits to be 3D, high resolution but slow and expensive.
- Optical elastography from microscopes to digital holography or Optical Coherence Tomography,that have very high resolution but are mostly surfacics.

Once the propagation of shear waves is imaged several methods exist to recover their local speeds. Straightfoward idea is to follow the wave front and measure the propagation time. This method is called time of flight and is used with fast imaging techniques such as ultrafast ultrasound, it can also be used with stromboscopic approach with slow imaging techniques like MRI or optical set-ups. An other emerging method is called noise correlation and is presented in details in section 1.3.

Comparison between quasistatic and dynamic approachs

Quasistatic approach (strain elastography) is widely available on ultrasound system, robust and provide high quality elastograms in real time. It has the unconvience to be qualitative, relatively low depth and often operator dependant [24].
On the other hand, dynamic approachs (mainly shear waves elastography) have limited availabilities and are hardly real time. However, they already provide high quality images, are less operator dependent and have the undeniable quality to be quantitative [24].

1.1.3. Challenges of elastography

This section's aim is not to be exhaustive on the challenges ahead, but to give the reader a glance on the future of elastography.
All elastographs available and most of ongoing clinical trials are making three major heavy

hypothesis:

- 1) Displacements are small enough for the problem to stay linear
- 2) Biological tissues are purely elastic
- 3) Biological tissues are isotropic

Research is focusing on going beyond thoses hypothesis.

1)By working in the non linear domain of strain one can distinguish with good contrast between benign and malignant tumor [18].

2)Furthermore, biological tissues can be highly absorbant, specially for frequencies above 20 kHz [34]. Voigt model for viscoelastic properties has been proven to fit absorption properties of soft tissues in low frequency range [13]. Experimental values of viscosity modulus in biological tissue have been measured in vivo for instance in liver [42].

3)Finally, biological tissue are often stratified tissues, far from isotropic. Figure 1.7 is showing the fibered structure of muscular tissue at any scale, making its viscoelastic properties highly dependant of fiber orientation. Shear waves speed highly depends of their propagation direction with respect to the fibers, and tends to travel 2 to 3 times faster in the fiber direction compared to normal fiber direction [60].

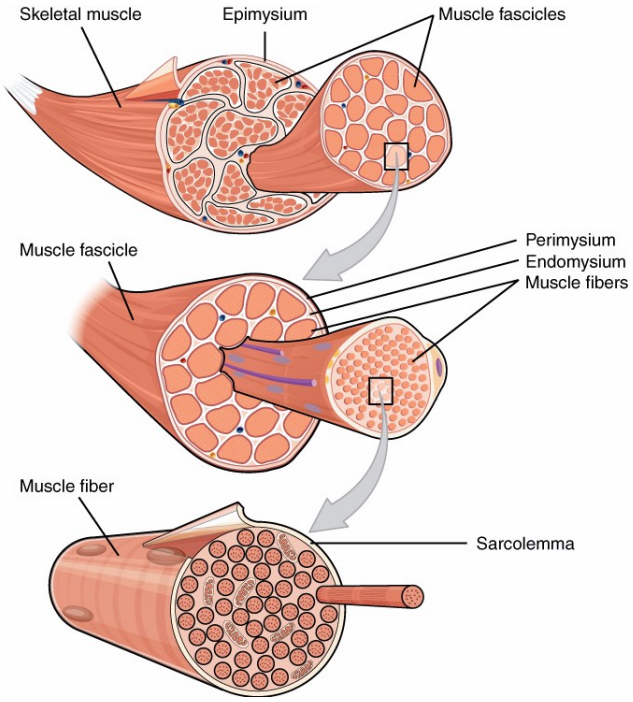

Figure 1.7: 3D structure of skeletal muscle tissue [7]

All those axes of researsh aim's at refining the modele by taking into account the viscoelastic behaviour's complexity of biological tissues.
Viscoelastic properties are determining for biological process at any scale, from macroscopic elasticity (whole liver harden by fibrosis) to subcellular elasticity. Diseases like malaria or cancer are for instance modifying cell's viscoelasticity [30]. With optical elastrography techniques like Brillouin's microscopy or simply transmission microscopes it's possible to map the elasticity of a single cell [54], [6] with promising application in cell's mechanic study.

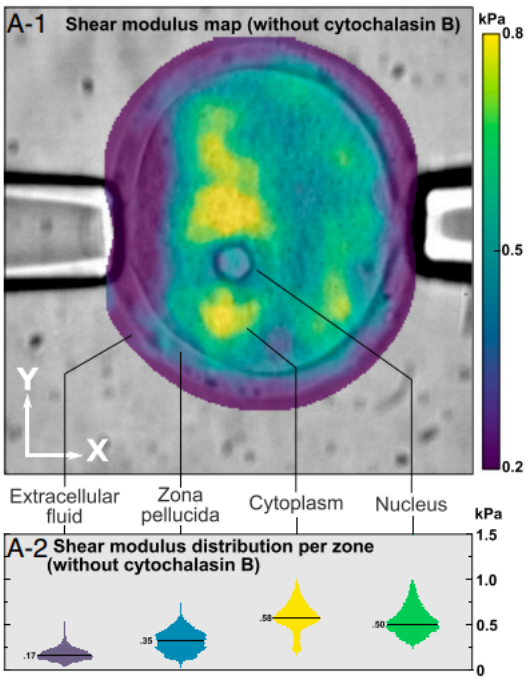

Figure 1.8: Optical elastography of a cell under vibration by transmission microscope taken from [6]

1.2. Continuum mechanics

From an acoustical point of view, biological tissues are inhomogeneous, scattering, highly absorbant solids often described as incompressible. They will be refered to as soft solids. In the section the propagation of elastic waves in tissue is described following the same structure than the highly recommended book from Royer and Dieulesaint [51].

1.2.1. First derivations

We assume a homogenous, unbound, purely elastic solid. For small strains ϵ, the stress σ is linked to strain by Hooke's law (1.2).The 81 components $c_{i,j,k,l}$ are called elastic constants.

$$\sigma_{i,j} = c_{i,j,k,l}\epsilon_{k,l} = c_{i,j,k,l}\frac{\partial u_k}{\partial x_l} \tag{1.2}$$

The mechanical displacement u, follows the equation of motion, that stand as 1.3 for an homogenous solid of volumic mass ρ with no volumic forces aplied.

$$\rho \frac{\partial^2 u(t)}{\partial t^2} = div(\sigma) \tag{1.3}$$

Combining equation 1.3 and 1.2, we obtain the propagation equation 1.4 where the three components of displacement are highly coupled.

$$\rho \frac{\partial^2 u(t)}{\partial t^2} = c_{i,j,k,l} \frac{\partial^2 u_k}{\partial x_j \partial x_l} \tag{1.4}$$

1.2.2. Isotropic purely elastic solid

The 81 components $c_{i,j,k,l}$ of Hooke's law are called elastic constants . Taking in account the symmetry of strain and stress tensors, the number of independant elastic constants is reduced to 21 [51] . In the case of an isotropic solid, the elastic tensor must be invariant by any plane or point symmetries or rotations. This reduces the number of elastic constants from 21 to 2 [51]. Those are called Lamé's constants, λ, μ. Considering this, equation 1.4 becomes 1.5

$$\rho \frac{\partial^2 u(t)}{\partial t^2} = (\lambda + \mu) grad(div(u)) + \mu \Delta u \tag{1.5}$$

To decoupled displacement components, let's use Helmholtz's decomposition, $u = u_L + u_T$ where u_L is irrotational and u_T has no divergence. Rewriting 1.5 with $\Delta u = grad(div(u)) - rot(rot(u))$ and applying the rotational 1.6 is obtained. Equation 1.7 is obtained applying the divergence.

$$\frac{\partial^2 u_L}{\partial t^2} - \frac{\lambda + 2\mu}{\rho} \Delta u_L = 0 \tag{1.6}$$

$$\rho \frac{\partial^2 u_T}{\partial t^2} - \frac{\mu}{\rho} \Delta u_T = 0 \tag{1.7}$$

The two equations 1.6, 1.7 are describing two uncoupled waves propagation. The first one (1.6) is longitudinal (see figure 1.9 type A). It's propagating with velocity $V_L = \sqrt{\frac{\lambda+2\mu}{\rho}}$, it's a compression wave, propagating irrotationaly. The second one (1.7) is transverse (see figure 1.9 type B). It's propagating with velocity $V_T = \sqrt{\frac{\mu}{\rho}}$, it's a shear wave with zero divergence. The two waves are propagating independently.

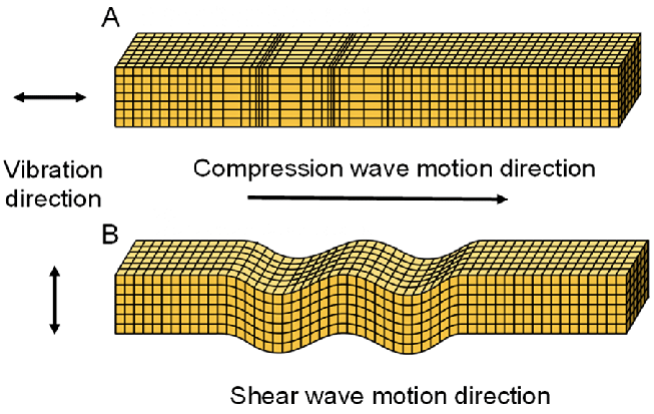

Figure 1.9: Shear and compression waves propagation [17]

1.2.3. Anisotropic purely elastic solid

For the general anisotropic case one must consider the 21 elastic constants and all the corresponding coupling described by the propagation equation 1.5. However, providing specific symmetries of the solid considered it exists a lot of case (orthotropic, monoclinic, cubic...), where the number of independent elastic constants disminish [51]. Due to their high stratification, biological tissues often present an axial symmetry. Muscle for exemple present an axial symmetry in the any planes of their fibers, and a rotation symmetry around the axis of the fibers. As the aim of elastography is to map biological tissues, let's focus our developpements on this type of symmetry called transverse isotropic.
Using the Voigt's notation, Hooke's law (equation 1.2) can be rewrited as a matrix product $\sigma = C\epsilon$ where C is the 6x6 stiffness matrix. Matrix C coefficients are simply a rewritting of the tensor's coefficient of elasticity $c_{i,j,k,l}$. For the transverse isotropic case, C takes the following expression [49]:

$$\begin{pmatrix} C_{1,1} & C_{1,2} & C_{1,3} & & & \\ C_{1,2} & C_{2,2} & C_{1,3} & & & \\ C_{1,3} & C_{1,3} & C_{3,3} & & & \\ & & & C_{5,5} & & \\ & & & & C_{5,5} & \\ & & & & & C_{6,6} \end{pmatrix}$$

Where $C_{6,6} = \frac{C_{1,1}-C_{1,2}}{2}$. Considering the fact that C is symmetric, the number of independant elastic constants is 5.

As for the isotropic case, the displacement obeys Newton's law, and the equation of propagation 1.5. When searching for solutions in the form of plane harmonic waves, it can be demonstrated that the equation of propagation allows 3 solutions with distinct phases velocities and polarization[49]. Explicite solutions can be found in[49]. The first root is a wave polarized purely transversely with displacements in the plane xOz (Figure 1.10 (b)) and propagate independantly from the other roots. The two other roots correspond to a "quasi" longitudinal compression wave and a "quasi" transverse wave with displacements in the nOy plane(Figure 1.10 (a)). The term "quasi" comes from the fact that those two waves are coupled in the general case and that their polarizations are not fully transverse or longitudinal[52].

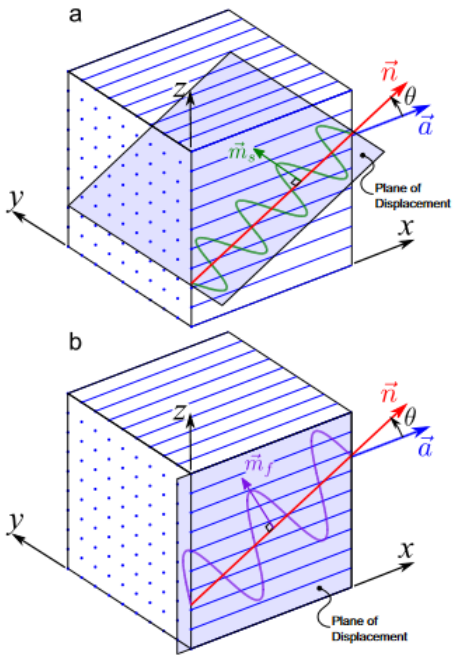

Figure 1.10: Two different types of transverses waves propagating in the tissues [57]. (a) purely tranversal waves, (b) "quasi" transversal waves

In the case of digital holography measurement, or laser speckle imaging the displacements measured are only displacements through the z directions. Therefore, the technique acts as a filter for the pure transverse waves. Only the pure tranverse waves will be detected and measured. Considering a plane harmonic wave propagating with purely transverse polarization, the following phases velocities (equation 1.8) can be retrieved. Phase velocities describe an ellipse in the plane of the fibers with a maxima in the direction of the fibers and a minima in the direction normal of the fibers. $C_{5,5}$ and $C_{6,6}$ are respectively called parallel shear modulus ($\mu_{\parallel}$) and perpendicular shear modulus ($\mu_{\perp}$).

$$\rho v_\phi^2 = C_{6,6} sin(\theta)^2 + C_{5,5} cos(\theta)^2 \tag{1.8}$$

The propagation is ruled by the following equation:

$$\rho \frac{\partial^2 u_T}{\partial t^2} - \frac{\mu_\parallel}{\rho} \frac{\partial^2 u_T}{\partial x^2} - \frac{\mu_\perp}{\rho} \frac{\partial^2 u_T}{\partial z^2} = 0 \tag{1.9}$$

1.2.4. Rayleigh waves

Optical set up focus on the surface of the sample or on its top layers. All previous derivations were made for the bulk of the sample, under the hypothesis of a sample infinite in all directions. In surface of the sample, considering that the long and large directions remains infinite, the propagation is still independant of frequencies. Wave velocity at the surface of the sample is not dispersive and still is an intrinsic parameter of the media. Lord Rayleigh in 1985 [11] set first the derivations of a surface wave in solid, with applications on sea surface and earthquakes. He left the waves his name.
Rayleigh waves propagating in surface dont resent the same stiffness than those in the bulk because of the presence of the free surface. Qualitatively, one can expect a reduced "effective" stiffness on surface waves with respect of the stiffness of the media driving waves in the bulk. Indeed, qualitatively waves in the surface (figure 1.11, cube A) resents 5/6 of the elasticity in the bulk (figure 1.11, cube B). Assuming that the velocity of transverse Rayleigh wave is of the form, $\sqrt{\frac{E}{\rho}}$, we can in first approximation link transverse Rayleigh waves velocity (V_R) and bulk shear waves by equation 1.10 (V_S)

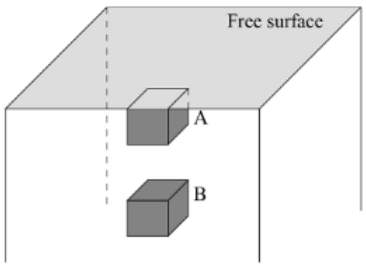

Figure 1.11: Cube A on the surface have 5/6 faces in contact with the stiffness of the media although cube B is embedded in it [51]

$$V_R = \sqrt{\frac{5}{6}} V_S \approx 0.91 V_S \tag{1.10}$$

In very first approximation Rayleigh waves can simply be considered as bulk waves propagating in an reduced "effective" stiffness media. For proper description on effect on polarisations, phase velocities the reader can refer itself to the book [50] . In the rest of this work we will assume transverse Rayleigh waves to behave like bulk shear waves and often mingle them under the name of shear waves.

1.3. Noise correlation or passive elastography

1.3.1. Introduction to noise correlation or passive elastography

Mechanical waves are propagating in the inside the human body due to internal movements created by heart beat, respiration, gastro-intestinal track... All this waves are scattered and reflected in the human body. It creates a noise-like field of low frequencies waves propagating in tissues. The so called noise correlation elastography or passive elastography aims at exploiting this natural field already present in vivo to measure elasticity in living organism. Figure 1.12 gives a example of this technique. An in vivo measure of the elasticity of the liver is realised without external excitation, only using noise field created by the patient homeostasis. Muscle and liver shear waves velocities are retrieved using an ultrasound system. Muscle is found to be stiffer than liver, as expected. We want to stress out that this measurement is obtain without any system of generation of waves in the tissue.

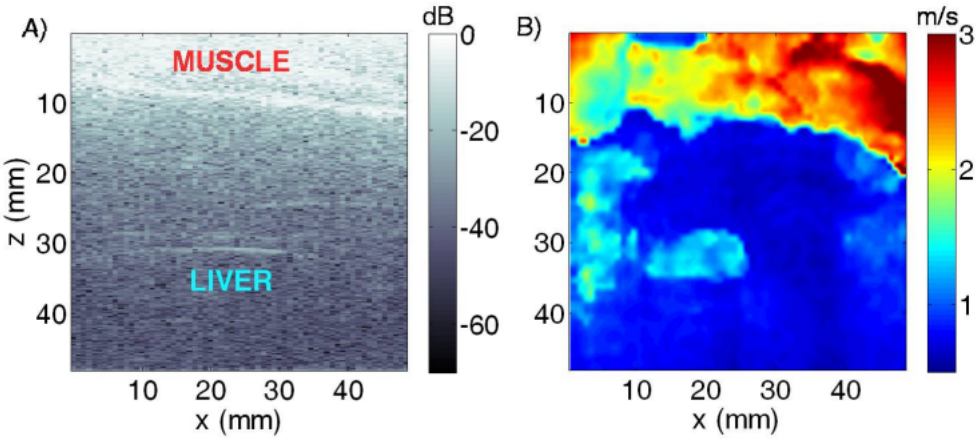

Figure 1.12: In vivo elastography in liver, (A) sonogram of the region of interest, the frontier between muscle and liver is visible, (B) corresponding elasticity retrieved by passive elastography, taken from [23]

We have seen that the velocity of the shear waves in the tissue can be linked with the elasticity of the tissue. In passive elastography, one use the naturally present wave field, and try to retrieve the local shear waves velocity in the tissues. But how from a diffuse wave field can we recover the velocity of waves? The answer was given by the field of seismology. Indeed, in the 2000's seismologist were able to extract residual wave speed and provide surface waves tomography from the ambient seismic noise [55]. It relies on correlation methods explained in details in this section.

1.3.2. Green's functions

Let's consider a differential linear operator L. A green function G is defined as a solution of the equation 1.11, where δ_s is the dirac function in the s position.

$$LG(x,s) = \delta(x-s) \tag{1.11}$$

Let's apply this to shear waves equation . Let's consider the following differential operator: $L = \frac{\partial^2}{\partial t^2} - \frac{1}{c^2}\Delta$. G(x,s), the green function is appearing as a solution of the wave equation for a point source placed in s. Let's assume that the green's functions are known for each point source s, one can now solve the general problem $Lu(x) = f(x)$ with u the displacement field and f the source field. Infact, f, the source field can be viewed as a sum of point sources placed in different positions. (equation 1.12).

$$f(x) = \int f(s)\delta(x-s)ds \tag{1.12}$$

That can be rewritten using equation 1.11, and the linearity properties of L to extract it from the integral.

$$f(x) = L\int f(s)G(x,s)ds \tag{1.13}$$

From equation 1.13, $u(x) = \int f(s)G(x,s)ds$ or more simply $u = G * f$. The solution of the general problem Lu=f is the convolution of the Green function with the source function. Solving the problem $LG = \delta$ gives access by superposition properties of the linear operator L to the solutions of $Lu = f$.
In the case of linear time-invariant system, a Green function of the system can be view as its transfer function in automatic.

1.3.3. Correlation of a field

Let's consider two source points A and B. $G_{\mathrm{a,b}}(t)$ is the transfer function between a and b in the time domain. Let's consider a source, s(t) in point S. The field $\Phi_{\mathrm{b}}(t)$ received in point B is $\Phi^s_{\mathrm{b}}(t) = G_{\mathrm{s,b}}(t) * s(t)$ where * represents convolution defined in equation 1.14.

$$(f * g)(t) = \int f(\tau)g(t-\tau)d\tau \tag{1.14}$$

The correlation between point A and B is defined in equation 1.15.

$$C^s_{\mathrm{a,b}}(\tau) = \int \Phi^s_a(t)\Phi^s_b(t+\tau)dt \tag{1.15}$$

Let's consider the following change of variable: $t' = t + \tau$. We obtain:

$$C^s_{\mathrm{a,b}}(\tau) = \int \Phi^s_a(t'-\tau)\Phi^s_b(t')dt' \tag{1.16}$$

Which can be rewritten considering the definition of convolution given in equation 1.14:

$$C^s_{\mathrm{a,b}}(\tau) = \Phi^s_a(-\tau) * \Phi^s_b(\tau) \tag{1.17}$$

In the case of a broader source, composed by multiple point source, by linearity the resulting correlation between point a and b will be $C_{\mathrm{a,b}}(\tau) = \sum_s C^s_{\mathrm{a,b}}(\tau)$.

Introducing the Green's fonction $\Phi^s_{\mathrm{b}}(t) = G_{\mathrm{s,b}}(t) * s(t)$ in equation 1.17 one can obtain equation 1.18.

$$C^s_{\mathrm{a,b}}(\tau) = G_{\mathrm{s,a}}(-\tau) * s(-\tau)) * G_{\mathrm{s,b}}(\tau) * s(\tau)) \tag{1.18}$$

The dirac δ being the neutral element of the convolution product, if the source sends an impulsion, $s(t) = \delta$ then $C^s_{\mathrm{a,b}}(\tau) = G_{\mathrm{s,a}}(-\tau) * G_{\mathrm{s,b}}(\tau) = G\mathrm{a,b}$. In the case of an impulse source the correlation between two point of a field is their Green's function.
However, if we demonstrated that $C^s_{\mathrm{a,b}}(\tau) = G\mathrm{a,b}$ for an impulse source, it's has no reason to be true in the general case.
Let's now consider a diffuse field.
By diffuse field, one intends a field of waves with random direction of propagation, random phases and random polarizations. This kind of field is obtain in multiple scattering media [35]. The autocorrelation of this kind of field tends to a dirac δ.
Equation 1.18 can be rewritten considering the commutativity of the convolution and the associativity of the Green's function in equation 1.19 where S is the autocorrelation of the source [41].

$$C^s_{\mathrm{a,b}}(\tau) = S(\tau) * G_{\mathrm{a,b}}(\tau) \tag{1.19}$$

In the case of a diffuse field, recovering $C^s_{\mathrm{a,b}}(\tau)$ the cross correlation between two points a,b is equivalent to measuring Green function $G_{\mathrm{a,b}}(\tau)$ linking them. From the correlation point of view, having a diffuse field around or impulse sources is equivalent.

Figure 1.13 illustrate the concept of correlation of point A with point B on numerical simulations [35]. A is chosen in the center of a cercle of 2900 impulse sources. In (a), (b), (c), the point A is fixed and the correlation $C_{\mathrm{a,b}}(\tau)$ is computed and displayed for each position of point B. The axial unit is the wavelength λ_0. In (b), the correlation is computed for $\tau = 0s$, we retrieve in point A the autocorrelation of the field in A. In (a), the correlation is computed for $\tau = -3T_0 s$, the field in point A is highly correlated with the field of points in the gray circle shifted back of $3T_0 s$. In (c), the correlation is computed for $\tau = +10T_0 s$. Let's now focus only on the point B represented by a triangle, in figure (d), one can notice that B have high correlation with point A for $-6T_0$ and $+6T_0$. Negative shift corresponds to the propagation from B to A, positive shift corresponds to the propagation from A to B. To go from A to B it takes the impulsion $6T_0$. Thanks

to this information the speed of the impulsion can be recovered if A and B positions are known.

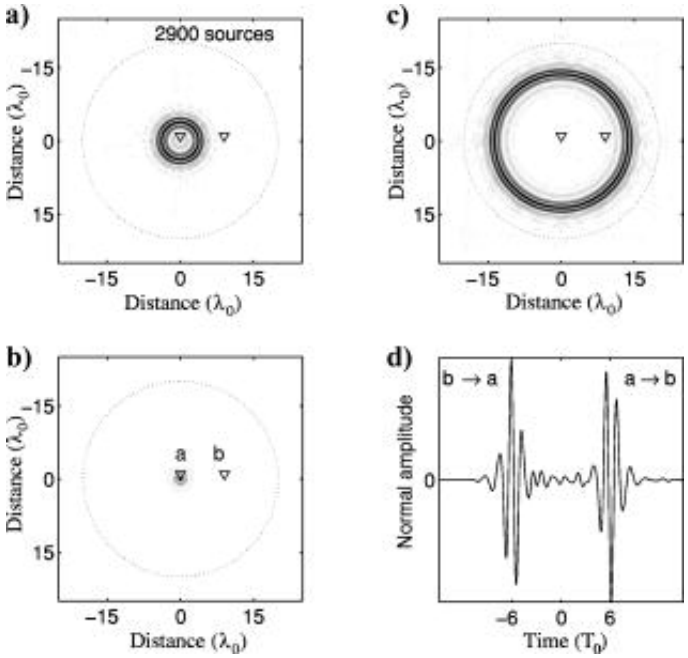

Figure 1.13: Simulation of temporal correlation between two points A and B in the center of a circle of gaussian sources of period T_0 emiting spheric waves. (a) correlation $C_{\mathrm{a,b}}(\tau)$ for $\tau = -3T_0$, (b) correlation $C_{\mathrm{a,b}}(\tau)$ for $\tau = 0$, (c) correlation $C_{\mathrm{a,b}}(\tau)$ for $\tau = +10T_0$, (d) correlation $C_{\mathrm{a,b}}(\tau)$ in point B. [35]

This example consider impulse sources but as demonstrasted earlier, from a correlation point of view it's equivalent to the same sources emitting a diffuse field.
To summerize previous statements

1. Correlation of a field and its Green function are closely linked by equation 1.19.
2. In the case of impulses sources or a diffuse field: correlation between two points is exactly their Green's function.
3. Knowing that, it's possible to follow the propagation on their correlation and to retrieve the wave velocity.

The gold standard for retrieving wave velocity in a medium is to use time of flight methods. By time of flight method one intends the tracking of a wave front in time. It's usually applied to raw film of wave propagation but it can also be applied on the correlation as demonstrated above. Following the propagation using correlation of the field is more accurate in the case of diffuse field. However, due to high waves velocities in tissue,

it requires high sampling frequency and large field of view to be accurate.
The strengh of the noise correlation technique is that it can overcome the sampling limitation and be applied to slow techniques like MRI, X rays, OCT scan... [13]. To understand it we have to interprete the correlation process as a time reversal experiment.

1.3.4. Time Reversal interpretation of correlation process

Time Reversal Mirrors

As derived previously acoustic waves are following Alembert's equation form (equation 3.1). It worths noticing two things. First space and time are playing similar roles in this equation, second it admits time symmetry (same solution for t and -t).

With a given set of initial condition the wave propagation follow a unique solution, time reversal mirror aims at refocusing this solution switching the arrow of time. In in a perfect time reversal mirror a set of antennas are embedded in the medium and are able to refocus acoustic waves as time was inverse. Time reversal (TR) experiments can be divided in two steps. In the foward step, the antennas are recording the incoming signal from the cavity. In the second step the field is retransmitted back to refocus in the same location it came from, following the exact same path [22].

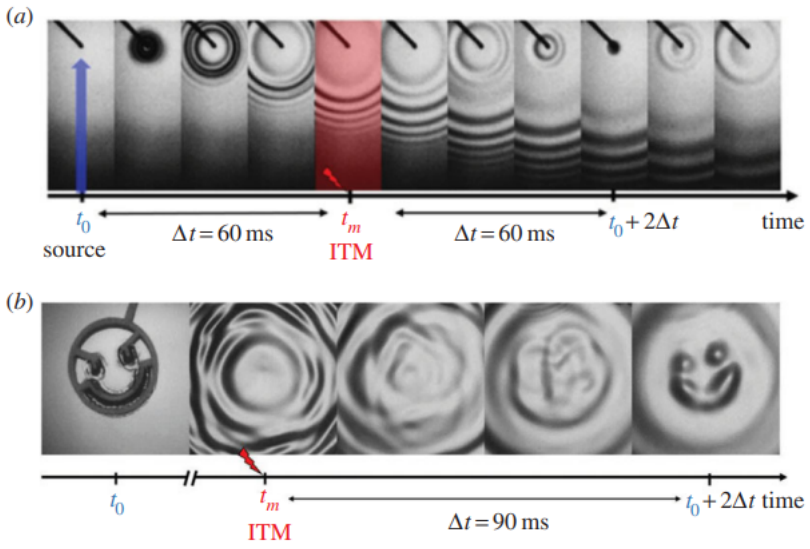

Figure 1.14: Instantaneaous time mirror (ITM) experiments with water waves, (a) for a point source, (b) for a complex source in smiley shape [22]

In figure 1.14, taken from [22], water waves experiments with instantaneous time mirror (ITM) are performed. In (a), at time t_0 a point source emits. It's recorded for δt, it's the foward step of the experiment. In t_m, the second step begins and the time mirror reemit back the recorded waves that refocus after $t_0 + \delta t$. The same experiment is repeated with a complex smiley source (b).

Link between time reversal of a field and correlation of a field

Looking at the correlations displayed in figure 1.13 the reader can qualitatively convince itself than $C_{\mathrm{a,b}}(\tau) = \phi_a^{\mathrm{TR}}(b,\tau)$ for impulse sources (or equivalently a diffuse field).Here $\phi_a^{\mathrm{TR}}(b,\tau)$ is the time reverse field of the field $\Phi_a(b,\tau)$. Indeed the part of the correlation with $\tau > 0$ corresponds to the foward step of the TR process (a point source is emitting in point A and propagate in the media) and the part of the correlation with $\tau < 0$ corresponds to the second step of the TR process, the waves refocus on point A.

Indeed it can be demonstrated [14] that the time reverse field ϕ^{TR} of any field ϕ following the wave equation verify equation 1.20.

$$\phi^{\mathrm{TR}}(b,\tau) = \Phi_a^s(-\tau) * \Phi_b^s(\tau) \tag{1.20}$$

In particular the displacements field E and the velocity field V of mechanical shear waves are following a wave equation of Alembert's form [14].

Their TR field verify equation 1.20. One can write equations 1.21 and 1.22

$$\epsilon^{\mathrm{TR}}(b,\tau) = E_a^s(-\tau) * E_b^s(\tau) \tag{1.21}$$

$$v^{\mathrm{TR}}(b,\tau) = V_a^s(-\tau) * V_b^s(\tau) \tag{1.22}$$

In other words, the correlation of a field is also its time reverse field for any field following Alembert's wave equation.

Link between time reversal of the displacement field and shear waves velocity

In one hand equation 1.23 can be demonstrated for a diffuse field [14]. It's valid only for t=0s.

$$c_{\text{shear}} = \sqrt{\frac{\epsilon^{\text{TR}}(b, t = 0s)}{v^{\text{TR}}(b, t = 0s)}} \tag{1.23}$$

In the other hand equation 1.24 and 1.25 can be derivated at first order [14].

$$\epsilon^{\text{TR}}(b, t = 0s) = \frac{\partial^2 C(t = 0s)}{\partial r^2} \tag{1.24}$$

$$v^{\text{TR}}(b, t = 0s) = \frac{\partial^2 C(t = 0s)}{\partial t^2} \tag{1.25}$$

Combining those two sets of equation one can derived equation 1.26 and equation where b is the receiver point.

$$c_{\text{shear}} = \sqrt{\frac{\frac{\partial^2 C_b(t=0s)}{\partial t^2}}{\frac{\partial^2 C_b(t=0s)}{\partial r^2}}} \tag{1.26}$$

To summerize, providing a diffuse field of shear waves, computing the correlation of this field in a given point gives access to the local spead of waves in this point.

1.3.5. Noise correlation applications in elastography

In elastography, the goal is to map the elasticity of the biological tissue. Shear velocity and elasticity modulus beeing linked by $E = 3\rho c_{\text{shear}}^2$, to measure elasticity one can measure shear waves velocity.

The noise correlation technique described above retrieves the shear waves velocity using the correlation at $t = 0s$ between a given receiver point and any other points. The strength of this technique is that it doesnt require a proper sample in time. Indeed, accordng to Shannon criteria, to image a 1kHz field of shear waves, the imaging technique should sample at least at 2kHz, that's incompatible with MRI, CT scans, most optical imaging techniques. The noise correlation technique doesnt require Shannon criteria to

be fulfill in order to retrieve shear waves velocity.

Not only noise correlation techniques is compatible with slow imaging it also allow for "passive" elastography. As explained earlier, in multiple scattering media, providing enough propagation time, the resulting obtained field is a difuse field. Noise correlation provides a robust and elegant method for elasticity retrieval.

2 | Laser speckle imaging elastography, state of the art

2.1. The speckle phenomenon

2.1.1. Introduction to speckle

On the order of the optical wavelength most of material are rough ($\lambda \approx 600nm \ll R \approx 1000nm$). When the beam hits the granular surface, it's reflected with a shift in phase and amplitude. LASER are highly coherent light with coherence length in the typical order of the meter. Scattered beams interfere with one another to produce a resultant intensity, that can be construtive or destructive. From an observator point of view the laser spot is "speckled", it presents a granular aspect due to dark and bright patterns (see figure 2.1)

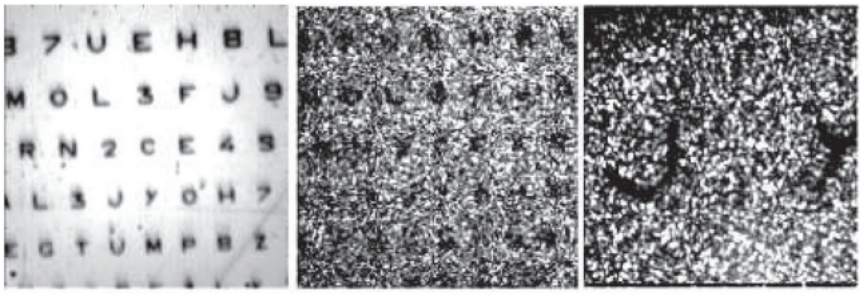

Figure 2.1: Illumination with incoherent light(a), illumination with coherent light (b), magnification of b (c) taken from [28]

Speckle is the phenomenon of diffuse reflection of coherent light through a rough object. Reciprocally, it's observed in transmission when a laser beam pass through a fine rough translucent object, acting as a diffuser.
Speckle is also observed outside of optic, for instance, in mechanical waves and radar waves. Waves are diffused by reflection and interfere creating a speckle pattern on image.

For imaging, speckle is thow consider as a noise and researcher aims at his complete removal. Figure 2.2 shows ultrasound image and figure 2.3 radar image presenting speckle noise.

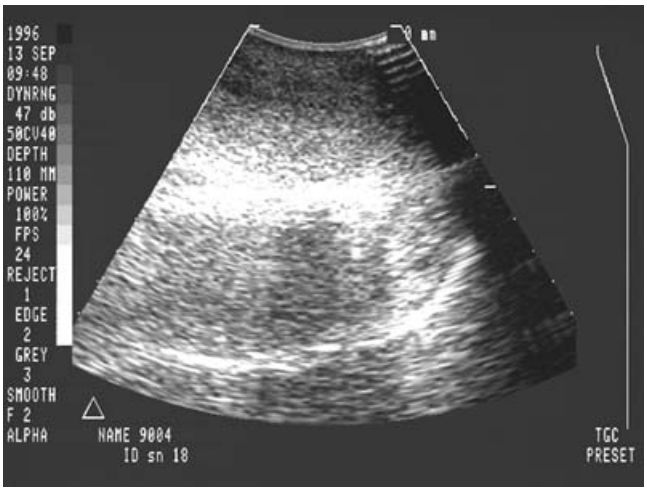

Figure 2.2: Speckled Ultrasound Image [3]

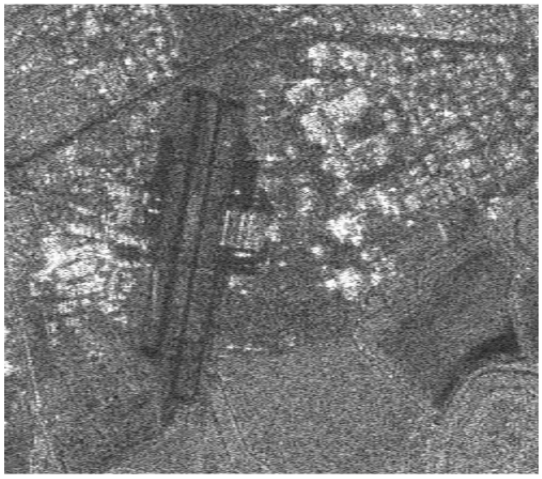

Figure 2.3: Speckled Radar Image on californian field [28]

However, speckle can also be view as a usefull tool to carry and extract information. It's used in metrology for vibrations, displacements, roughness measurements [4] or image processing([48]).

2.1.2. Statistical properties of the speckle

If the reader own a LASER pointer, by pointing it to a rough surface (anything else than a mirror) and observing the speckle pattern, one can observe than dark spots are

more numerous than bright ones. In this section we will describe first order statistic for amplitude and phase of the diffused speckle. We will then pass from this amplitude,phase statistics to a resulting intensity statistic more usefull in an optic application.

Phase and amplitude statistics

Let's consider diffuse reflection of coherent light on a rough surface as in figure 2.4. Each wavelets are reflected with a shift in amplitude and phase. Considering the variation of height of the surface random, the problem is a random sum of phasors (figure 2.5). The sum can result in an constructive (case (a)) or destructive (case (b)) phasor.

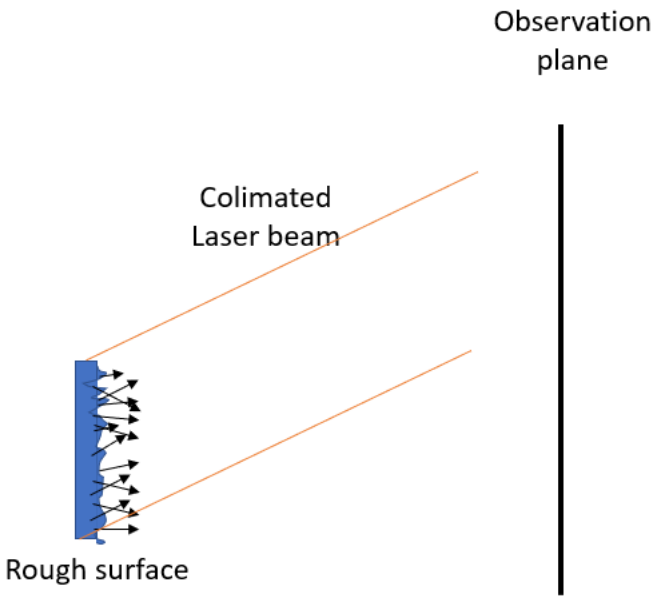

Figure 2.4: Speckle observation set-up

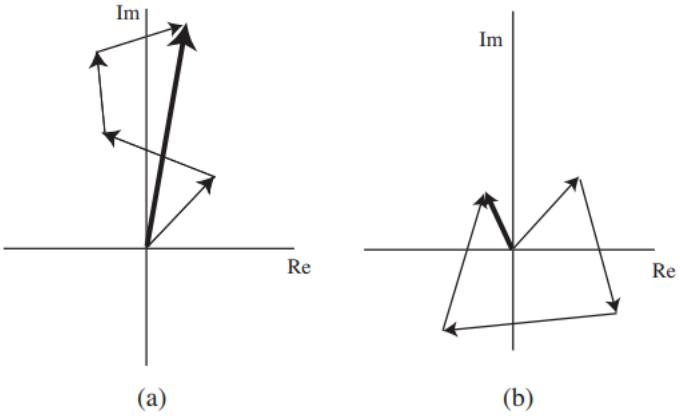

Figure 2.5: Random sum of phasors representated in the imaginary plane. (a) constructive addition, (b) destructive addition [28]

The resultant phasor A, sum of N phasors of amplitude a_n and phase ϕ_n is expressed equation 2.1.

$$A = a \exp j\phi = \frac{1}{\sqrt{N}} \sum_{n}^{N} a_n \exp j\phi_n \tag{2.1}$$

The following hypotesis are made: each phasors in the sum are independant from each others, in a single phasor amplitude and phase are independant to each other. Finally we assume a random distribution of the phase in [-π: π].
In the imaginary plane, this problem is similar to a random walk problem where phasor amplitudes and phases are equivalent to step length and direction angle.
Using this analogy, it can be demonstrated [28] than the real and imaginary part of the resultant phasor A are tending when N $\Rightarrow \infty$ to a gaussian statistic. One can then demonstrate that the resultant phasor's amplitude has a Rayleigh density distribution (equation 2.2).
The phase is following an uniform density distribution in [-π: π] (equation 2.3)

$$p_A(A) = \frac{A}{\sigma^2} \exp -\frac{A^2}{2\sigma} \tag{2.2}$$

$$p_(\phi) = \frac{1}{2\pi} \tag{2.3}$$

Intensity statistic

Intensity is defined as a fonction of amplitude $I = f(A) = A^2$. From probability joint theory one can write: $p_I(I) = p_I(A^2) = p_A(\sqrt{I})\frac{dA}{dI}$. Finally equation 2.4 is linking amplitude density probability to statistics of intensity.

$$p_I(I) = p_I(A^2) = p_A(\sqrt{I})\frac{1}{2\sqrt{I}} \tag{2.4}$$

Using equation 2.2 in 2.4 we obtain the probability of density of intensity of the resultant phasor. It's a negative exponential law (equation2.5) characterized by a standard deviation equal to the mean value.

$$p_I(I) = \frac{1}{\langle I \rangle} \exp -\frac{1}{\langle I \rangle} \tag{2.5}$$

In our specific speckle case it implies that degree of fluctuation around the mean value is in the same range that the mean value itself.

Let's define contrast as in equation 2.6.Under our hypothesis it's equal to one, this type of speckle will be refered as fully developped. A lot of reason can decrease contrast, main one being the uniform phase distribution. A speckle with C<1 will be refered to as partially develloped.

$$C = \frac{\sigma_I}{\langle I \rangle} \tag{2.6}$$

We assume that having several random walkers doesnt change much to their final points compare to the case where they are walking alone ie random walkers do not have any interaction force and they can step on each other. Indeed, it can be demonstrated[28] that the sum of resulting phasors behave statistically the same than a single resultant phasor. All the precedent derivations were made only for a single resultant phasor in one space point. Results found in the section for a single point speckle will hold true for a complete pattern.

2.1.3. Spatial structure of speckle

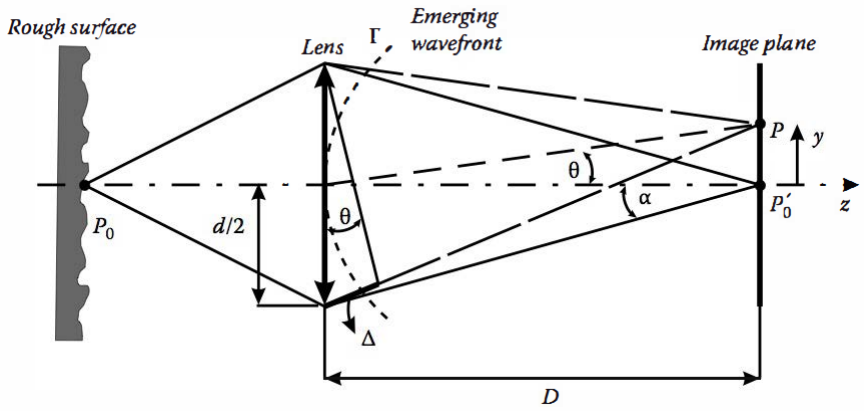

Figure 2.6: Optic scheme of the plane extension of a speckle dot [48]

We want to derive the spatial extension of a single dot in a speckle pattern. Let's consider a speckle pattern observed through a lens in the image plane (see figure 2.6). P_0' is the image of a single point P_0 of the surface. D is the distance between the image plane and the lens, α is the numerical aperture of the lens. The point P of the image plane is situated at a lateral distance of y from P_0'.
Waves arriving in P present a phase shift with respect with the ones arriving in P_0'. Γ is the emerging wavefront just after the lens. The path difference in the image plane is $\Delta = dsin(\theta) \approx dy/D$

Let's P_0' be the center of a speckle dot and P the border so that δ the lateral extention of the dot is $\delta = 2y$. P and P_0' are part of the same diffraction figure: $\Delta << \lambda$. For the border point P we obtain $\delta = 2\lambda D/d$ Lateral extension simply depend of the numerical aperture of the system and the wavelength of the laser (equation 2.7)

$$\delta = \frac{\lambda}{\alpha} \tag{2.7}$$

Similarly, let's derive the axial extension of a single speckle. P_0' is the image of a point on the surface in the optic axis, P_0'' is a point on the optic axis situated at δz before (see figure 2.7. Let's call I the intersection of the emerging wavefront (Γ and the lens border ray.
Following [48] the path difference between in the image plan π' including point P_0'' is $\Delta = \delta z \frac{\alpha^2}{2}$. To be part of the same diffraction pattern $\Delta << \lambda$. Defining δz the border of

the diffraction spot, the axial extention of the speckle pattern follows equation 2.8.
The axial and lateral extention of a single speckle dot only depend of the wavelength of the light and the numerical aperture of the system. There is no dependance of the illuminated rough surface.

$$\delta z = 4\frac{\lambda}{\alpha^2} \tag{2.8}$$

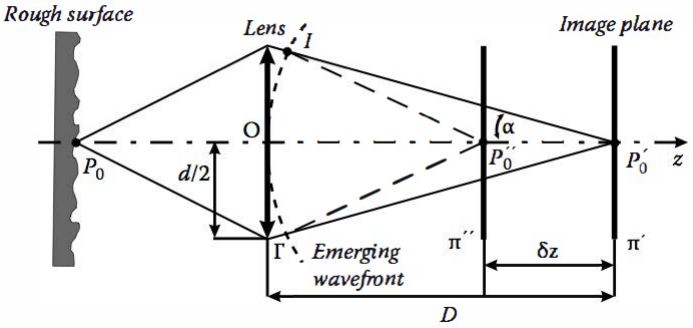

Figure 2.7: Random sum of phasors representated in the imaginary plane. (a) constructive addition, (b) destructive addition [28]

2.1.4. Speckle as a carrier of information

Speckle pattern results of a random summation of phasors, it's intrisically a statistical process. The statistic of intensity drawing a speckle pattern depends of two factors: the characteristic of the surface and the coherence of the light beam. For a given Laser and a fixed surface, it's independent of time, this case is refered to as static speckle. On the contrary, any change in the diffusive surface (translations, vibrations, change of refractive index, change of absorption index...) or in the illumination (drop of coherence length, addition or removal of incoherent / coherent lights sources, change of the angle of illumination...) will modify the speckle statistic. This space-time dependance of the speckle is refered to as dynamic speckle. Here follows a list of some applications.
With a fixed illumination, and an unactive surface change of speckle statistics is directely related to mouvements of the surface. It's possible to detect and distingush translation, rotation in the samples. The following article gives an overview of this kind of speckle sensor used for instance in computer mouse [61].
Providing a static and unactive surface, illumination of the sample with a moving angle gives access to roughness measurement and to the surface topography. The speckle statistic of intensity can be modeled as a function only dependent of the incident angle and the

roughness of the surface. This technique being rapid, noninvasive and nondestructive it founds many industrial applications main one being the detection of damage and failure in mechanical part [31].
With a fixed illumination and unmoving sample, time dependance of speckle statistic properties can be linked to the activity of sample. Activity refers to any change in light-matter interaction in the sample. Reflexion, scattering, absorbtion, reradiation properties of the sample if they change will modify speckle statistic. For instance, drying of paint on a sample will modify its reflective index, flow circulation in the sample causes scatterers to move... Living sample in particular shows high activity, and are giving a boiling, bubbling speckle aspect. Therefore, speckle patterns with high variability are refered to as "biospeckle" or "boiling" speckle. One of many example of application of this biospeckle in non destructive approach for food quality and safety detection [43].

2.1.5. Method for dynamic speckle analysis

As described in the previous section, dynamic speckle properties can carry various informations. This section's aim is to present how to link the dynamic speckle properties to the information to be retrieve.

2.1.6. Spatial contrast

As derived in the previous section the intensity's density of probability of the speckle follow a decreasing exponential trend (Equation 2.5). One consequence is that the mean intensity equals its standard deviation. The speckle is then refered to as fully develloped and has a contrast of one (equation 2.6).
Changes in the illumination or in the sample will causes the speckle contrast to decrease. Let's take for instance the addition of a constant phasor (uncoherent light) to a fully develloped speckle, $A = A_0 + A_n$. The amplitude of the constant phasor (A_0) will be add to the random addition of diffused phasors ($A_n = a_n \exp(\theta_n)$). A_n is following a gaussian density of probability (equation 2.2) [28].The intensity of the resulting phasor will contain an interference term (equation 2.9). It will no longer have a decreasing exponential density the contrast will drop under 1. The speckle is partially develloped.

$$I = A_0^2 + A_n^2 + 2A_0A_n cos(\theta) \tag{2.9}$$

Change in the speckle contrast is dependent not only on the illumination but also on the

surface characteristics such as roughness or activity. If we add frame of static speckle, the correlation between them will be high and the summed contrast will be high. On the contrary if the speckle is dynamic, for instance presents areas of activity, the images will be less correlated and activity areas will presents drop of contrast. Contrast is a measure of sample activity.

2.2. Transient elastography by Laser speckle imaging

Speckle contrast is a measure of the sample activity. Local speckle contrast drops with movements of the scatterers. In particular, when waves propagates at the surface of the sample, they cause the scatteres to move in their polarization direction. This creates a drop in speckle contrast allowing the imaging of the wave propagation. X. Chen and team, in [16] are using laser Speckle contrast to retrieve not only elasticity but also viscosity of Oil-in-Gelatin Phantoms. They use transient elastography i.e. they send an impulse wave and follow its propagation in the sample. In the set-up used in figure 2.8, (a). Laser propagates through a lens to focus on a CMOS camera. Impulse wave is transmitted to a speaker drived by a function generator. Stromboscopic approach is used to increase the sampling frequency. The maximal sampling frequency of the camera is 1kHz, using a simultaneous trigger for the camera and for the piezo impulse (b), they reach an effective sampling frequency of 20 kHz.

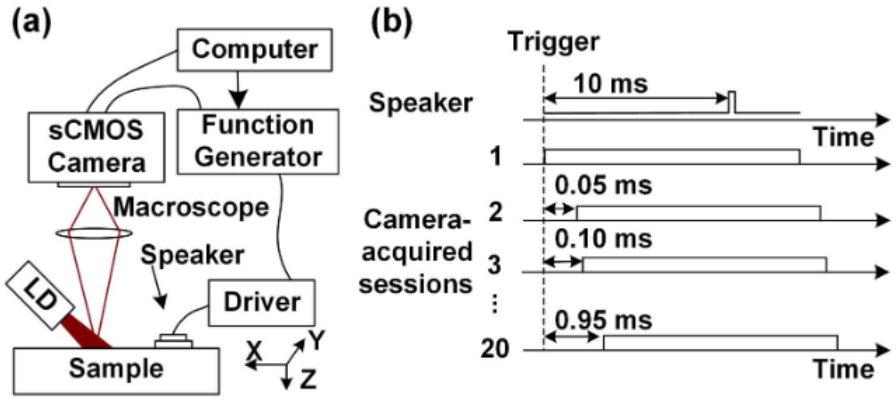

Figure 2.8: (a) Schematic of the experimental set-up. (b) Trigger sequences of the camera and speaker, taken from [16]

The speed of the wave carries elasticity information (μ_1), in other hand, the amplitude loss, or distance of propagation carries the absorption information (μ_2). Results are displayed in figure 2.9, reference values are provided by a rheometer. A good compliance is found with the rheometer values. The more oil is in samples the more viscous and absorbant it

becomes.

	Pulse		Rheometer	
Oil Type	**μ_1(KPa)**	**μ_2(Pa · s)**	**μ_1(KPa)**	**μ_2(Pa · s)**
0%	1.13	0.31	0.78 ± 0.06	0.16 ± 0.02
10%	2.52	0.48	1.00 ± 0.03	0.49 ± 0.06
20%	3.59	1.55	1.05 ± 0.03	0.80 ± 0.08
40%	1.03	2.88	0.89 ± 0.05	1.81 ± 0.03

Figure 2.9: Elasticity Modulus μ_1 and Viscosity Modulus μ_2 of Oil-in-Gelatin Phantoms, taken from [16]

This point we want to stress out from this study is the possibility to retrieve viscoelasticity properties from laser speckle imaging.

3 | Simulation of elastic waves propagation by finite differences method

3.1. Setting up the simulation

This section's aim is to construct a Finite Difference Method (FDM) simulation of 2D elastic wave propagation. For an isotropic homogenous medium, displacements follow 3.1.

$$\frac{\partial^2 u}{\partial t^2} - c^2 \Delta u = s(t) \tag{3.1}$$

Let's look for an approximate 2D solution on the following domain: [0, Lx]x[0,Ly] and [0, T]. The domain is meshed with spatial steps δx and δy and time period sampling δt. According to Taylor's formula 3.2, for small displacements variation, we can discretize the wave equation 3.1 to obtain 3.3. i,j are indexing x,y directions and k is indexing time, $\gamma_x = c^2\delta t^2/\delta x^2$, $\gamma_y = c^2\delta t^2/\delta y^2$.

$$f(x+\delta x) = f(x,t) + \delta x \frac{\partial f(x)}{\partial x} + \delta x^2 \frac{\partial^2 f(x)}{\partial x^2} + o(\delta x^2) \tag{3.2}$$

$$u_{i,j}^{k+1} = 2u_{i,j}^k - u_{i,j}^{k-1} + \gamma_x[u_{i-1,j}^k + u_{i+1,j}^k - 2u_{i,j}^k] + \gamma_y[u_{i,j-1}^k + ui + 1, j^k - 2u_{i,j}^k] \tag{3.3}$$

At $t = 0^-$ s the medium is at rest, initial speed is null, $u_{i,j}^2 = u_{i,j}^1$.

At each iteration, wave sources are imposed $u_{sx,sy}^{k+1} = s(sx, sy, k+1)$. The goal is to simulate a diffuse field of displacement, broadband in frequency. To do it, sources are chosen with a white spectrum on a given frequency interval as in figure 3.1. Sources are placed all around the mesh every 10 spatial steps.

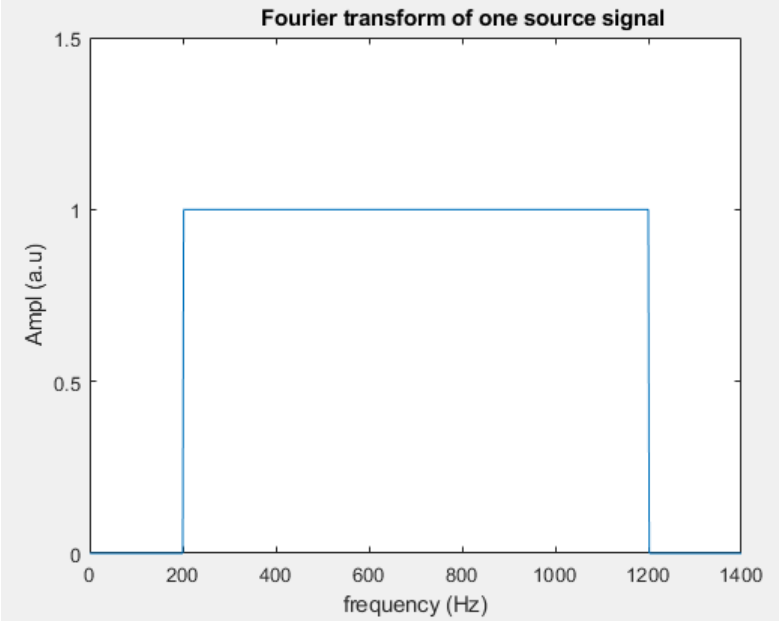

Figure 3.1: Spectrum of a source placed on the border of the mesh

Global scheme of the mesh is given in figure 3.2

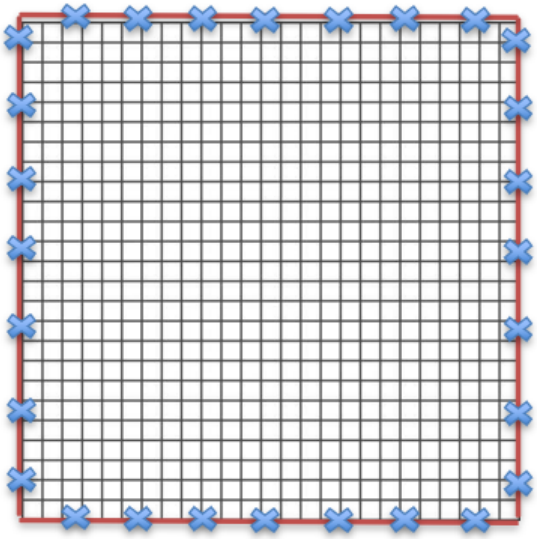

Figure 3.2: Mesh scheme, red line are absorbant boundaries, blue cross are sources of waves

To avoid parasite reflexion, boundaries conditions (3.4) are chosen absorbant The border at time k+1 take the value at time k of the line of pixels just before the border. $n_x =$

$L_x/\delta_x, n_y = L_y/\delta_y$

$$\begin{aligned} u(1,:,k+1) &= u(2,:,k) \\ u(:,1,k+1) &= u(:,2,k) \\ u(n_x,:,k+1) &= u(n_{x-1},:,k) \\ u(:,n_y,k+1) &= u(:,n_{y-1},k) \end{aligned} \tag{3.4}$$

This aborbing boundaries aren't completely absorbant, but in our case, are sufficient to prevent resonance in our cavity.

3.2. Simulation of shear waves propagation in an isotropic soft media

Let's consider an isotropic, homogenous, purely elastic solid of volumic mass ρ. Elastic constants are reduced to only two, the Lamé constants λ, μ. Two waves are propagating in the solid, one is longitudinal (bulk wave), one is transversal (shear wave). As demonstrated in section 1.2, those two waves propagate independently following wave equation of Alembert's form (equation 3.1). Their velocities are defined as:

$$V_L = \sqrt{\frac{\lambda + 2\mu}{\rho}}$$

$$V_T = \sqrt{\frac{\mu}{\rho}}$$

In soft medium, $\lambda >> \mu$, velocity of bulk wave is far above velocity of shear wave $V_L \approx 1500m/s$, $V_T \approx 10m/s$. At the same frequency the wavelength of longitudinal wave is approximately 150 times the wavelength of shear wave. On the scale of shear wavelength only shear waves are propagating in the tissue. Therefore, the FDM simulation described in the former section can be applied for shear waves simulation.

The following parameters are chosen:

$$c_s = 3m/s$$

$$L_x = 50mm, L_y = 50mm$$

$$\delta_x = 100\mu m, \delta_y = 100\mu m, \delta_t = 20\mu s$$

The waves simulated are displayed in figure 1.1 in the following link: `https://polimi365-my.`

sharepoint.com/:p:/g/personal/10783888_polimi_it/EQ-mnaP0YCFBgCwLRT5-Wr8BEGwXd9uc9wZnKMA
e=CD9cXl. The correlation between central point and all the other points for $\tau \in [-4ms : 4ms]$ of the simulated field is computed in figure 1.2 of the previous link. In particular the correlation for $\tau = 0s$ is displayed in figure 3.3.

Summary of results of section 1.3.

1. A diffuse field is equivalent from the correlation point of view to an impulse source.
2. There is an equivalence between the temporal correlation of a field and the time reverse version of the field.
3. If the field is diffuse, the correlation for $\tau = 0s$ is the focal spot in acoustic, the equivalent of the point spread function (PSF) in optic of the point where the correlation is computed.
4. In the general case, the correlation for $\tau = 0s$ is the impulse response of the field convoluted with a term dependent on the source's form (see equation 1.19).

The correlation of the field for $\tau = 0s$ is the point spread funtion (PSF), the focal spot of the wave fields in this point. With analogy to the diffraction process, there is a link between the radius of the focal spot (r_0), the wavelength of waves in the media 3.5, and the numerical aperture of the wave field. Then, by knowing the central frequency of the field (f_0), the velocity of shear waves can be retrieved $c = \lambda f_0$. Equivalently, the velocity can be derived from the equation 1.23.

$$a \approx \frac{\lambda}{\alpha} \tag{3.5}$$

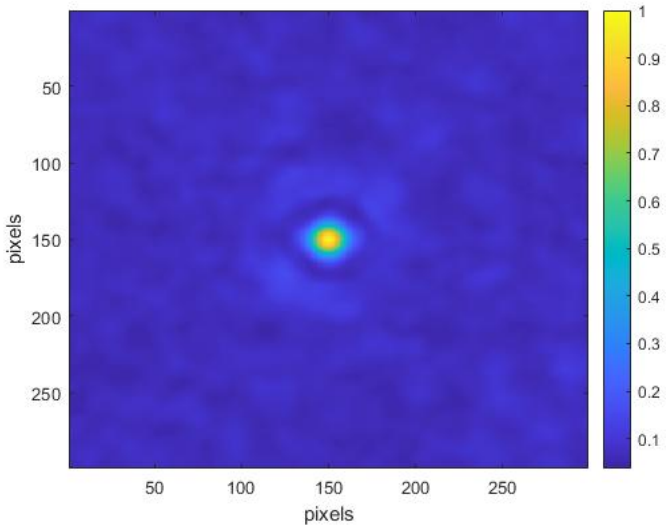

Figure 3.3: Point spread function in the center of the simulated isotropic medium with c=2m/s. One pixel is 20 μ m. Amplitude is in arbitrary unit

3.3. Simulation of shear waves propagation in an anisotropic soft media

Now, considering an anisotropic tissue following incompressible transversely isotrope hypothesis described in chapter 1.2 with $c_{\parallel}, c_{\perp}$ velocities of the shear wave in the axe of the fiber and perpendicularly to them. As derived in chapter 1.2 , the shear waves propagation follows a wave equation in the form of equation 1.9 . That can be discretized as equation 3.3, but unlike in the isotropic case, in the anisotropic case, $\gamma_x = c_{\parallel}^2 \delta t^2 / \delta x^2$ is different from $\gamma_y = c_{\perp}^2 \delta t^2 / \delta y^2$.

The following parameters are chosen:

$$c_{\parallel} = 2.5m/s, c_{\perp} = 2m/s$$

$$L_x = 50mm, L_y = 50mm$$

$$\delta_x = 100\mu m, \delta_y = 100\mu m, \delta_t = 20\mu s$$

The waves simulated are displayed in video 2.1 in the following link: `https://polimi365-my.sharepoint.com/:p:/g/personal/10783888_polimi_it/EQ-mnaP0YCFBgCwLRT5-Wr8BEGwXd9uc9we=CD9cXl`.

The correlation between central point and all the other points for $\tau \in [-4ms : 4ms]$ of

the simulated field is computed in video 2.2 of the previous link. In particular the correlation for $\tau = 0s$ is displayed in figure 3.4. The PSF exhibits two different wavelength 3.5 according to the direction corresponding to two different velocities $c_\perp, c_\parallel$.

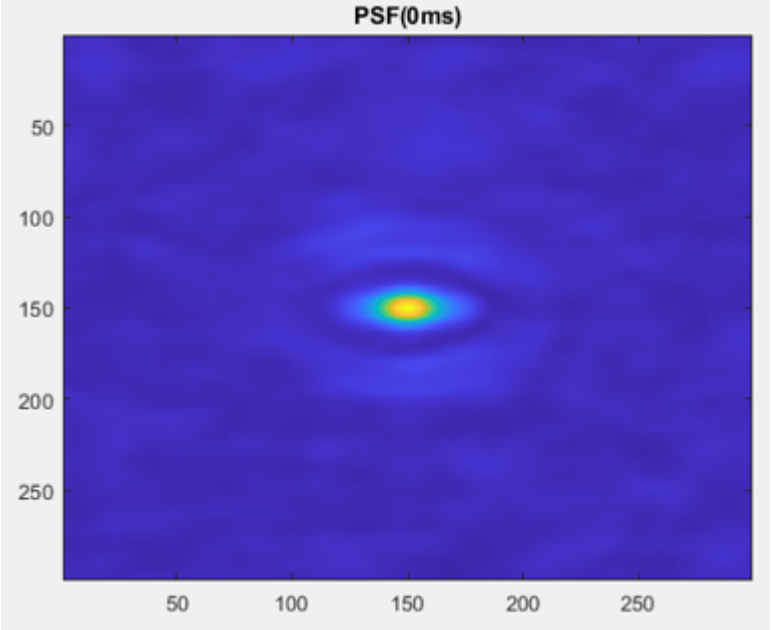

Figure 3.4: Point spread function in the center of the simulated anisotropic medium with $c_\perp = 2m/s$ and $c_\parallel = 2.5m/s$. Amplitude is in arbitrary unit

Using equation 1.23 on simulated data, we recover $c_\perp = 2m/s, c_\parallel = 2.5m/s$.

3.4. Simulation of shear waves propagation in an isotropic soft media with anisotropic distribution of excitation sources

Now, considering the same situation described on section 2.2, an isotropic media with a shear velocity of $2m/s$. In section 2.2 the sources of shear waves were distributed homogenously around the mesh (see figure 3.2). Providing the fact that the sources s(t) are emitting a diffuse field $S(t) = \delta$, with S the autocorrelation $s(t) * s(t)$.
In this section the sources are only on the lower part of the mesh. The simulated field is displayed in video 3.1. The correlation between central point and all the other points for $\tau \in [-4ms : 4ms]$ of the simulated field is computed in video 3.2. In particular the correlation for $\tau = 0s$ is displayed in figure 3.5. $S(t)$ the autocorrelation of the sources is no more a δ for every point of the field. The effect on the correlation of the field for

$\tau = 0s$ is an elongation perpendicular to the excitation.

The correlation for $\tau = 0s$ cannot be considered anymore as straightfowardly as the point spread function (i.e. impulse response) of the field. Indeed as derived in section 1.3, $C^s_{\mathrm{a,b}}(\tau) = S(\tau) * G_{\mathrm{a,b}}(\tau)$.
Nevertheless in the direction of the propagation $S(t) \approx \delta$, and a measure of velocity is still possible. Indeed, we retrieve c=2 m/s using equation 3.5 in the direction of propagation.

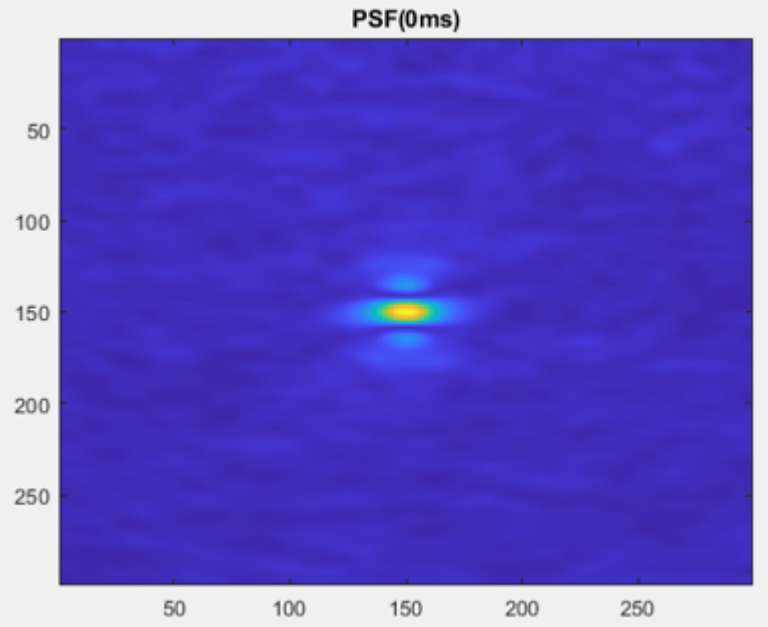

Figure 3.5: Correlation of the field for $\tau = 0s$ in the center of the simulated isotropic medium with c=2m/s, with an unbalanced repartition of the field. Amplitude is in arbitrary unit

3.5. Problematic exposition

To recover local waves speed, noise correlation algorithm compute local correlation of the wave field. Trough an interpretation of the correlation as the point spread fonction (PSF) of the media in this point, and a analogy with time reversal field, it's possible to retrieve the shear waves velocity in the point of interest (see section 1.3). Under the assumption of an isotropic excitation, the correlation's shape is a circle in isotropic media (case (a)), an elongated ellipse for an anisotropic media(case (b)). It's then possible to recover speeds and elasticities in differents directions of propagation. The large axes direction of the ellipse will correspond to the high speed direction. Velocity measurement is based on the shape of the point spread function. A straightfoward idea to distinguish between isotropic

and anisotropic media is to draw their PSF, a circular PSF correspond to isotropic media and elliptic one to an anisotropic media.
However, the correlation of an isotropic media with anisotropic distribution of the excitation sources will be an ellipse as well (case (c)), even tough the media is perfectly isotropic. The shape criteria isn't robust enough.
Furthermore, in this specific case the correlation at $\tau = 0s$ is not exactly the point spread function, but is biaised by the source distribution.

As in experimental condition the repartition of the excitation sources is not always isotropic, the shape of the PSF criteria is not robust enough to drive conclusions on the anisotropy properties of a tissue. The aim of this section is to find a classification algorithm able to distinguish between an isotropic tissue, an anisotropic tissue and an anisotropic distribution of the excitation sources.

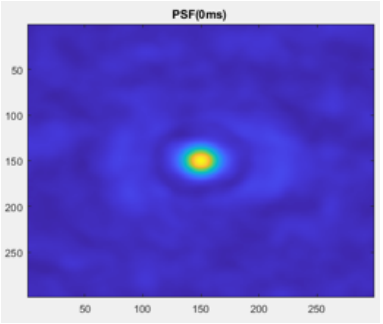

(a) Isotropic tissue

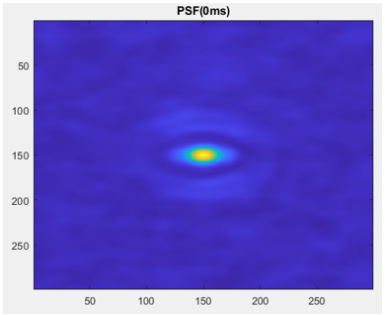

(b) anisotropic tissue

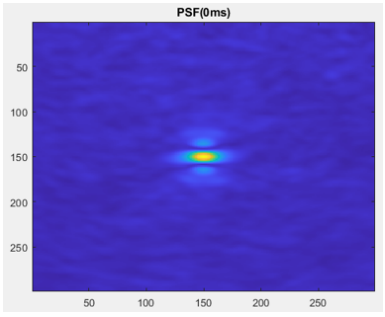

(c) anisotropic distribution of the sources

Figure 3.6: Point spread function simulations in the three cases of interest

3.6. Classification solver

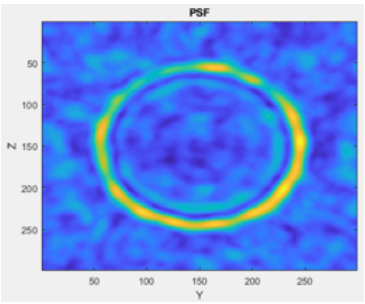

(a) Isotropic distribution of sources, correlation field for $\tau = 150ms$

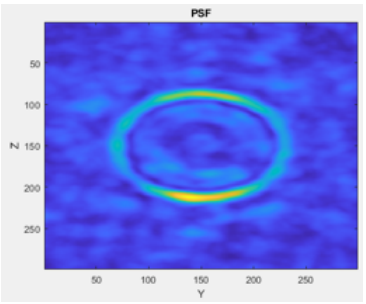

(b) Anisotropic media, correlation field for $\tau = 150ms$

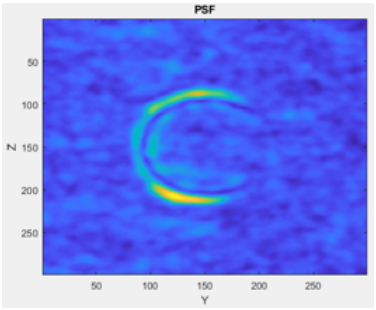

(c) Anisotropic distribution of sources, no sources on the right border, correlation field for $\tau = 150ms$

Figure 3.7: Point spread function simulations during propagation in the three cases of interest

3.6.1. Energy distribution criteria

Correlation of the field in the differents cases of interest for $\tau = 150ms$ are displayed in the next page.

If the excitation sources are not isotropically distributed, the energy distribution during the propagation will be anisotropic. In case (b), as there are no sources on the right part of the mesh, no energy is coming from there.

By dividing the correlation in 8 zones with an equal quantity of pixels, each one corresponds to an angle of $\frac{\pi}{4}$ around the point where the correlation is computed. Energy is all different, 8 zones are computed by adding the zone's pixels values. Let's call S the symmetry index of a correlation pattern, defined as the variance of the 8 zones energy (equation 3.6).

$$S = var(E_i) \tag{3.6}$$

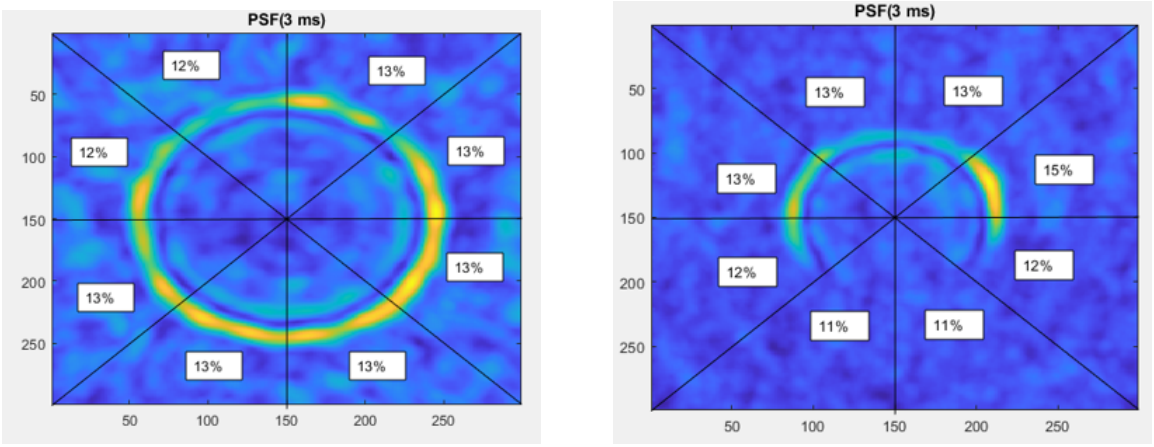

(a) Isotropic distribution of sources, $S = 0.0034$

(b) Anisotropic distribution of sources, no sources on the bottom border, $S = 0.012$

Figure 3.8: Energy distribution for different positions of the sources

Having a large S index means that we are facing an inhomogenous energy distribution during propagation. Therefore, a large S index points on an anisotropic sources distribution.

To compute the S index, the algorithm takes the correlation during the propagation and projects it in polar coordinates(r,θ) by interpolation. Then it computes the sum for each θ intervals of the integral on the radius.

3.6.2. Ellipse criteria

Figure 3.6 displays the correlation for $\tau = 0s$ for the 3 classes to distinguish. If the media is anisotropic, the correlation will be an ellipse whereas in the isotropic case it will be a circle. To quantify how far an ellise is from a circle, a straightfoward idea is to look at the large and small diameter of the ellipse and to compute their ratios (see figure 3.9). Let's call this ratio C, the ellipse criteria defined in equation 3.7.

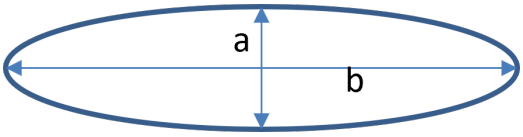

Figure 3.9: Ellipse with a,b respectively the large and small diameter.

$$C = \frac{b}{a} \tag{3.7}$$

C equals to 1 means that we are facing a circle, therefore, is the case of an isotropic tissue. On the other hand, C $<$ 1 means that we have an ellipse and points to any kind of anisotropy.

To compute C, the algorithm takes as input the correlation for $\tau = 0s$, and projects it in polar coordinates (r,θ) by interpolation. Then it computes for each θ the first value of 'r' to fit a threshold condition (Pixel value $<$ 0.2Max). The minimum value of 'r' will be the small diameter, the maximum value of 'r' will be the large diameter.

3.6.3. Decision tree

The following decision tree (see figure 3.10) is proposed and implemented. As input, it takes two parameters: the correlation computed in $\tau = 0s$ and the correlation computed in τ different than 0s, (i.e. in the propagation part of the correlation). As output, the decision tree provides one class between isotropic medium, anisotropic medium and anisotropic distribution of the sources. To do so, it computes two index, S the symmetry index, and C the ellipse index. S and C are compared to arbitrary thresholds T_1,T_2.

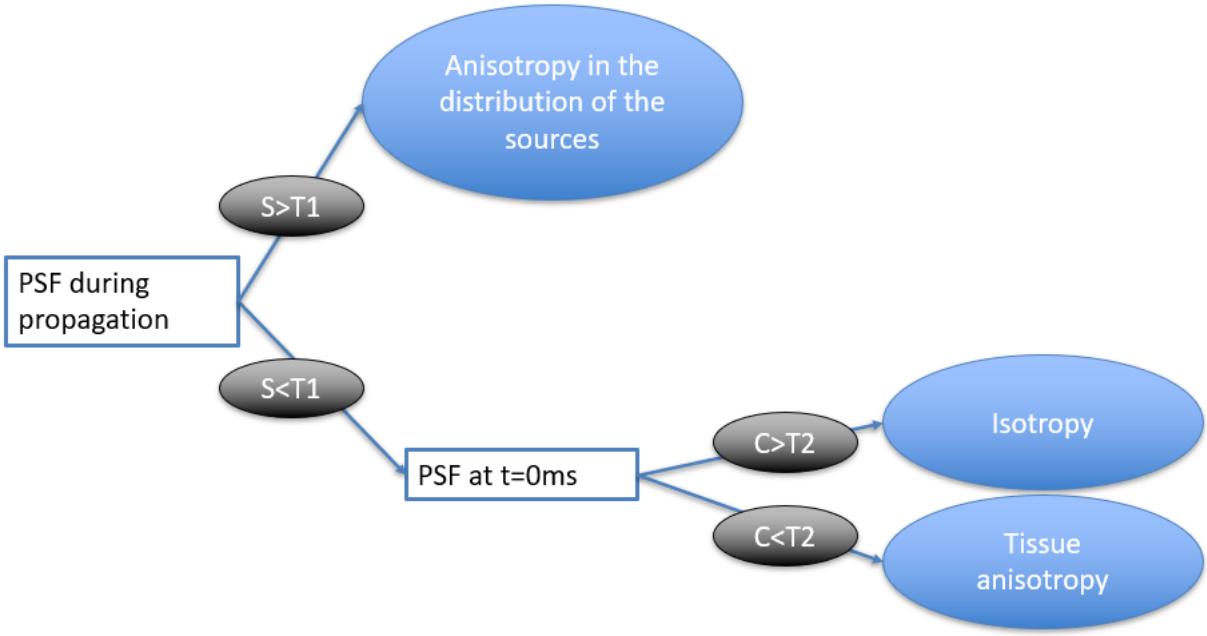

Figure 3.10: Decision tree, S (symmetry index) is defined in equation 3.6, C (ellipse index) is defined in equation 3.7, T1,T2 are arbitrary thresholds

3.6.4. Results

Case	Isotropy 2m/s	Isotropy 2.5m/s	Isotropy 3m/s	Anisotropy of tissue 2/2.25 m/s	Anisotropy of tissue 2/2.5m/s	Anisotropy of tissue 2/2.75m/s	Anisotropy of tissue 2/3m/s	Anisotropy of tissue 2/4 m/s	Anisotropy of sources N=1/2	Anisotropy of sources N=1/4	Anisotropy of sources N=3/4
S	0.0061	0.0048	0.0034	0.0098	0.0062	0.0062	0.012	0.012	0.017	0.035	0.012
C=b/a	1.375	1.4	1.333	1.86	2.14	2.43	-	-	-	-	-
Decision tree results	Isotropy	Isotropy	Isotropy	Anisotropy of tissue	Anisotropy of tissue	Anisotropy of tissue	Source anisotropy	Source anisotropy	Source anisotropy	Source anisotropy	Source anisotropy

Figure 3.11: Results

The proposed classification algorithm is tested on simulations for different shear waves velocities, ratio of $c_\perp/c_\parallel$, source distributions (N is the digital aperture of the distribution). Results are accurate except in the case of highly anisotropic medium with $c_\parallel/c_\perp >> 1$. Indeed, it can be seen in figure 3.12, that the energy repartition is not similar in the slow and fast axes. This unbalanced repartition gives a high S and a high variance of the energy repartition, having an effect on the algorithm to fall into an anisotropy of sources (see decision tree 3.10.

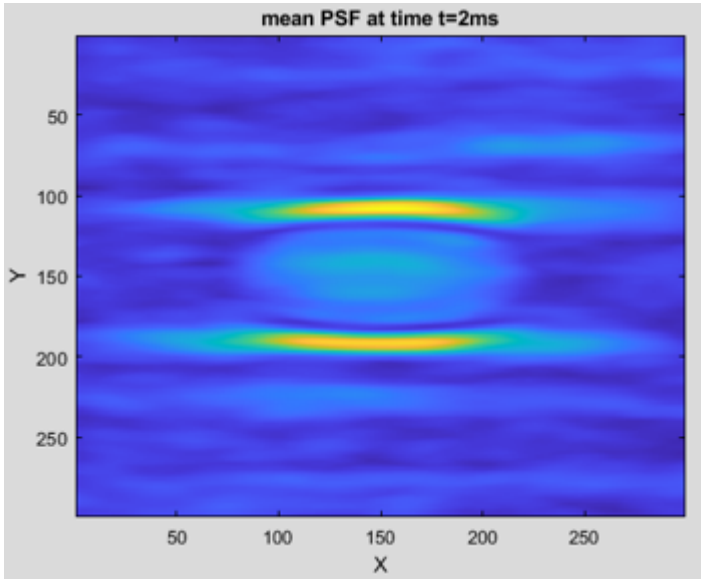

Figure 3.12: PSF during propagation for an highly anosotropic medium, S=0,012

Let's introduce a new index, 'AS', standing for axial symmetry index. It's defined as the upper part on the bottom paret times the left part on the right part of the point spread function.

$$AS = \frac{\sum_{\theta=0}^{\pi} E_\theta}{\sum_{\theta=\pi}^{2\pi} E_\theta} \frac{\sum_{\theta=-\pi/2}^{\pi/2} E_\theta}{\sum_{\theta=\pi/2}^{3\pi/2} E_\theta} \tag{3.8}$$

This index indicates if the energy distribution during propagation exhibits an axial symmetry. Indeed, this symmetry criteria separates the large ellipse with inhomogenous energy repartition between fast and slow axes (see figure 3.12) from inhomogenous energy repartition due to anisotropic distribution of the excitation sources (see figure 3.8, case (c)).

Corrected decision tree including this new index is proposed in figure 3.13. Results on simulations with new algorithm are displayed in figure 3.14. The algorithm shows excellent results with 100% of accuracy.

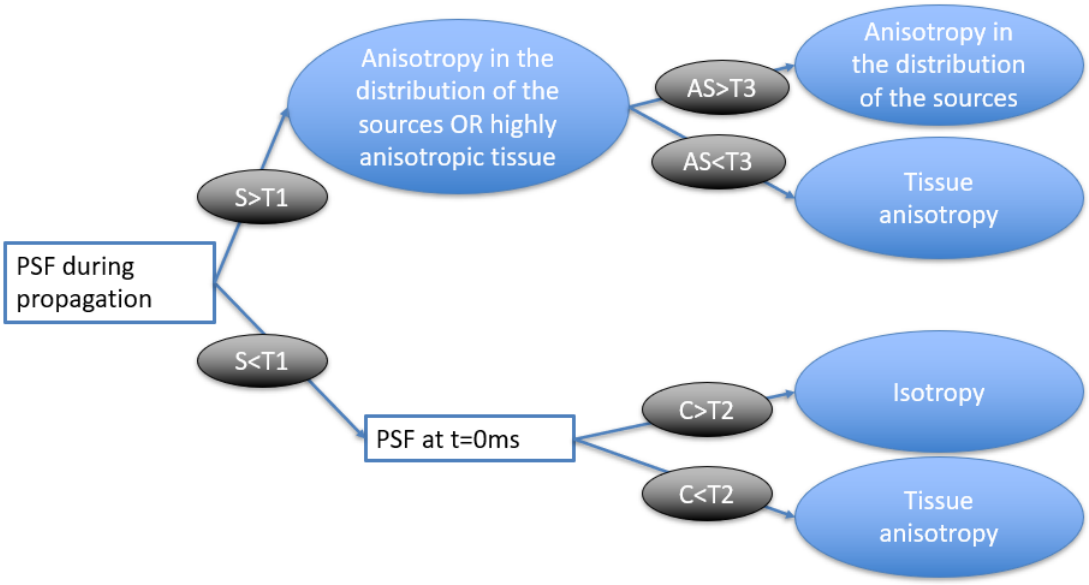

Figure 3.13: Decision tree for classification, S (symmetry index) is defined in equation 3.6, C (ellipse index) is defined in equation 3.7, AS (axial symmetry index) is defined equation 3.8. T1, T2, T3 are arbitrary thresholds

Case	Isotropy 2m/s	Isotropy 2.5m/s	Isotropy 3m/s	Anisotropy of tissue 2/2.25 m/s	Anisotropy of tissue 2/2.5m/s	Anisotropy of tissue 2/2.75m/s	Anisotropy of tissue 2/2.75m/s	Anisotropy of tissue 2/4 m/s	Anisotropy of sources N=1/2	Anisotropy of sources N=1/4	Anisotropy of sources N=3/4
S	0.0061	0.0048	0.0034	0.0098	0.0062	0.0062	0.012	0.012	0.017	0.035	0.012
C=b/a	1.375	1.4	1.333	1.86	2.14	2.43	-	-	-	-	-
AS							1.02	1.01	0.72	0.66	0.86
Decision tree results	Isotropy	Isotropy	Isotropy	Anisotropy of tissue	Anisotropy of tissue	Anisotropy of tissue	Anisotropy of tissue	Anisotropy of tissue	Source anisotropy	Source anisotropy	Source anisotropy

Figure 3.14: Results with corrected algorithm

3.6.5. Choice of thresholds

Results in the above section are obtained with the following thresholds: $T_1 = 0.01$, $T_2 = 1.6$, $T_3 = 0.08$. At a first attempt the thresholds were arbitrarily fixed in order to optimize the results of the algorithm. To put threholds on trial, a gaussian noise with a signal to noise ratio (SNR) of 2 was applied to the simulated data, and the diferent correlations in input of the algorithm were computed. The thresholds were then optimized to provide accurate results even in the noisy data.

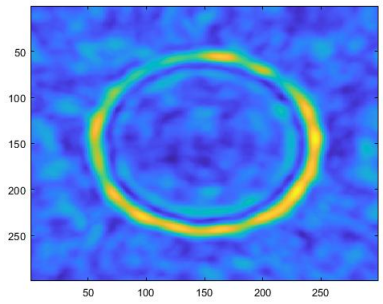

(a) Isotropic tissue, correlation during propagation, no noise

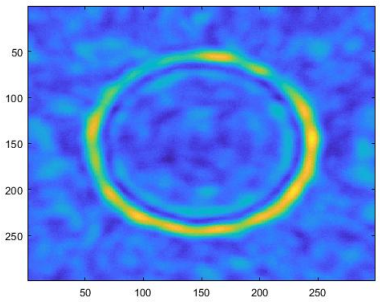

(b) Isotropic tissue, correlation during propagation, gaussian noise SNR=2

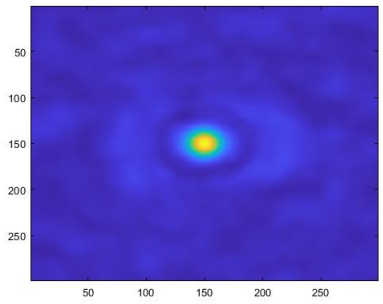

(c) Isotropic tissue, correlation for $\tau = 0s$, no noise

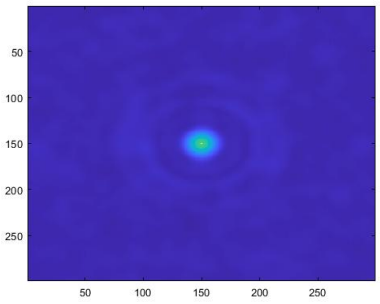

(d) Isotropic tissue, correlation for $\tau = 0s$, gaussian noise SNR=2

The PSF computed on noisy data are displayed in the above figure. The correlation during propagation is almost unchanged in the noisy case (b) with respect to the reference one (a). In the other hand, the correlation for $\tau = 0s$ is noticeably impacted with reduction in intensity of the correlation between points close to the center (case (c) and (d)). Temporal correlation of two gaussian noise signals is theoretically a dirac. The only point where the noise is surviving the correlation process is the point where $\tau = 0s$.

3.7. Simulation's conclusion

Finite difference simulations of elastic waves have been implemented. Noise correlation methods has been illustrated on isotropic and anisotropic samples. Different distribution of the excitation sources have been tested. A bias in the anisotropy measure of stiffness has been highlighted: the anisotropy in the distribution of the excitation sources around the receiver point prevents the measure by noise correlation method. A classification algorithm has been proposed and implemented, able to detect this situation and distinguish it from real tissue anisotropy.

4 | Elastography by laser speckle imaging

4.1. Introduction

Through simulation of elastic waves propagation the following statements have been demonstrated.
First, correlation of a diffuse field of waves allows to retrieve waves velocity in the media and its elasticity.
Second, in mechanically anisotrope media, the mechanical anisotropy ratio can be retrieved, but only if the diffuse field is isotropically distributed around the point of interest.
The case of an anisotrope diffuse field can be detected provided the computation of 3 different indexes and being discarded from other cases.
Waves have been simulated in a 2D plane, displacements are filtrated on the normal axis to the plane, in plane, the displacements are set to 0. The experimental configuration is mirroring the simulation. Indeed, Laser speckle imaging performs a 2D measure of waves propagating with normal polarization with respect to the surface plane. The most important difference is the sample rate. The camera used during the experiment is not fast enough to allow a proper sampling of waves frequency of propagation. To overcome this issue, two concurrent approaches will be used: stromboscopic sampling of impulses and noises correlation.

The experiment aims to show that one can perform mechanical anisotropic properties measurements by noise correlation method. To provide experimental proof the workflow is described as the following steps:

1. Verify the ability of Laser Speckle Imaging to retrieve with good result the elasticity of Agarose samples using the gold standard method of time of flight. Mechanically isotropic and anisotropic agarose samples will be characterized.

2. Retrieve elasticity of agarose samples using correlation of a diffuse field method, taking as comparison the gold standard method.
3. Underline experimentally the bias in the measured velocities of waves with anisotropic distribution of the diffuse field sources.
4. Show that the previous situation can be detected and then avoid to follow the former proposed decision tree.

4.2. Material

4.2.1. Set-up description

The laser used is a semiconductor laser uncollimated of power 82mW. A CMOS camera (Basler aceA2040) of 2048px *1536 px and pixels of 120μm is used with its maximal sampling frequency 112Hz and an exposure time of 200μs. The objective used (Navitar) has a 25mm focal and an aperture of 1.4. To generate shear waves in samples an amplified piezo actuator (Cedrat technologie APA100M-19-008) is driven by a function generator (Tecktromic AFG1062). To generate diffuse wave field piezoelectric patches are used (REF) driven by pulse width modulation and an arduino board.

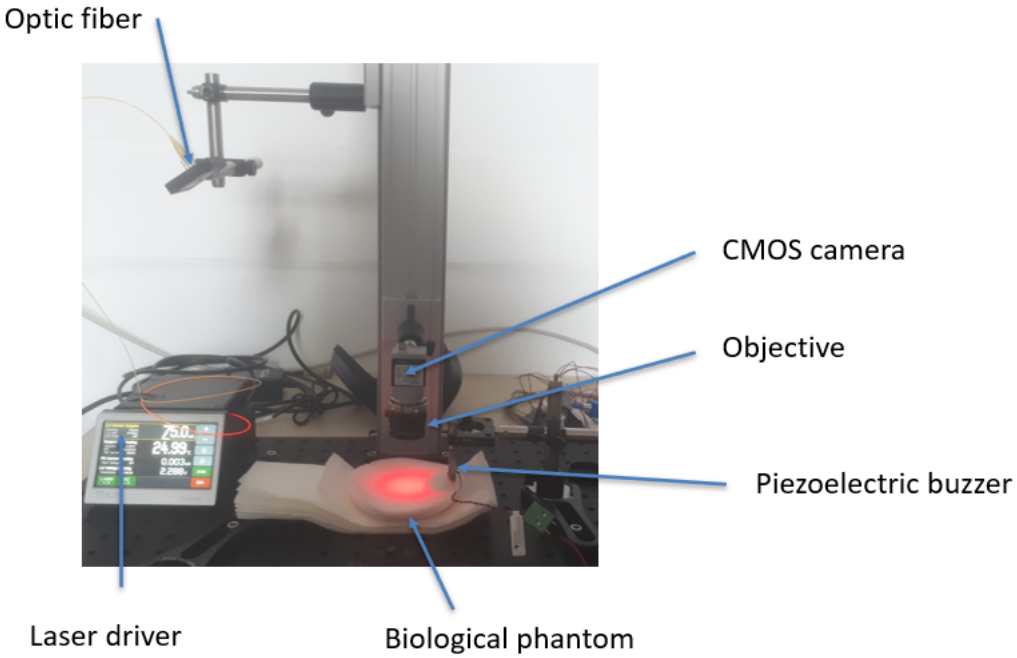

Figure 4.1: Picture of the set up used in the lab

Picture 4.1 shows the experimental set-up. A schematic of it is drawn in figure 4.2. Laser is powered by a laser driver and pass through an optic fiber. The laser beam hits the biological sample with a tilt angle. The speckle pattern is imaged by an objective and registered on a CMOS camera sending data to the computer. An exemple of the acquired image is given in figure 4.3. Pixels are 28 μm large and the entire field of view is 5.7cm * 4.3cm. The numerical aperture of the objective is set to 1.4, its maximum.

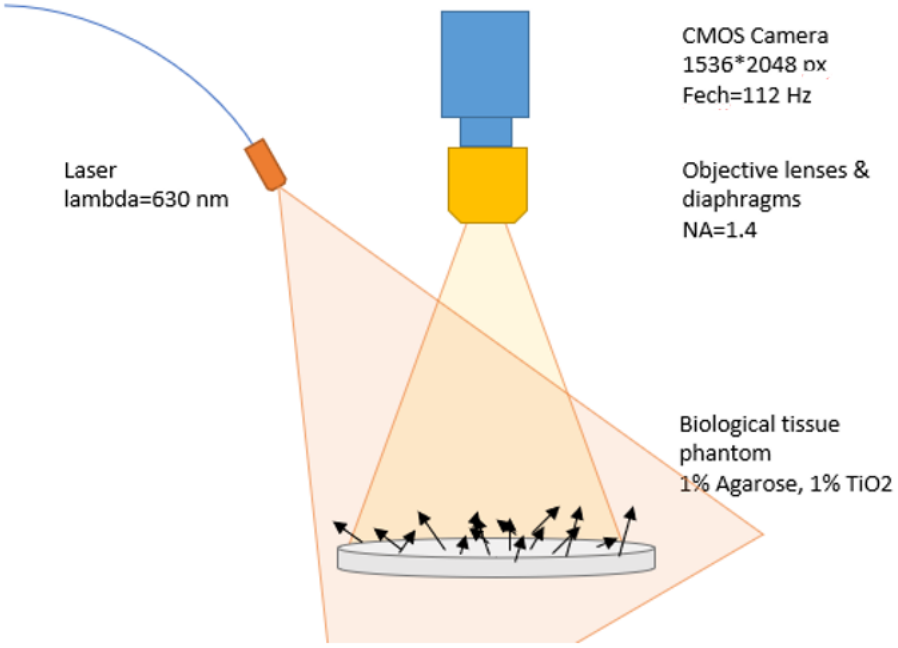

Figure 4.2: Scheme of the set up used in the lab

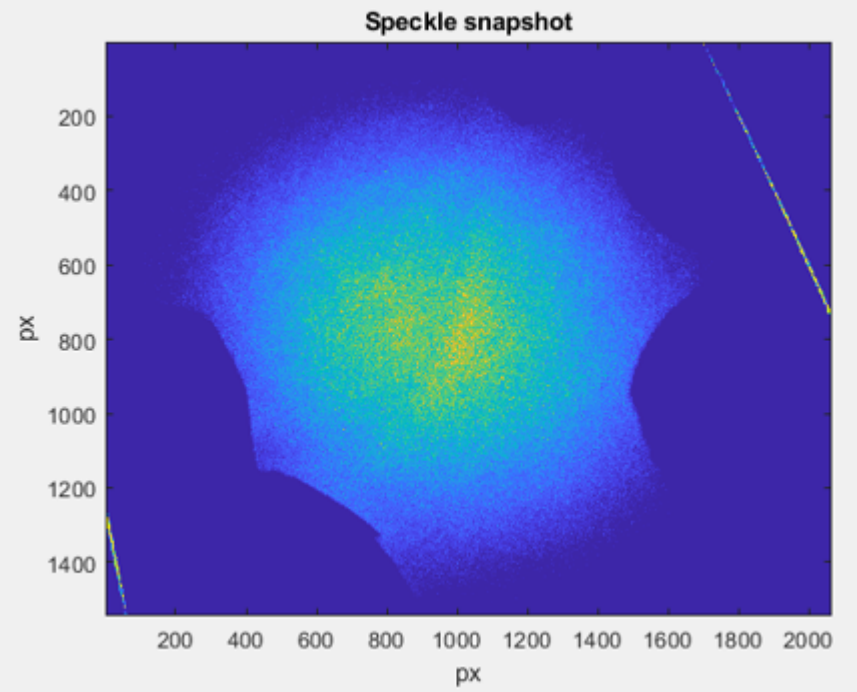

Figure 4.3: Raw acquired image, the field of view is 5.7*4.3 cm, one pixel is 28*28 μ m

4.2.2. Preparation of samples

Samples are made out of Agarose(A9539, Sigma-Aldrich, St. Louis, Missouri) with mass concentration between 0.5% and 1%, and TiO2 nanoparticles (277370010, Acros Organics, Morris Plains, New Jersey) with mass concentration of 1%. Agarose and water mix were heated under constant agitation then poured into a recipient. The samples were cooled at 4 C° for 1 hour to obtained a solid circular sample of 10cm diameter. Obtained elasticity are between 1 and 100 kPa [40] providing good comparison with biological soft tissues [53].
Anisotropy in the sample was created using sewing wire. The wire was streched on the recipient before the agarose mix was poured. It was streched in only one direction. Once the sample is cooled, a final layer of agarose is poored and cooled on the surface to make sure the wire is recovered and embedded in the agarose matrix.

4.3. Methods

4.3.1. Processing of raw speckle images

To obtain waves propagation from collected speckle images, two processing steps are applied. First differences of succesive images is performed to obtain a differential stack D

(equation 4.1 with I(n) the nth image acquired).

$$D(n) = I(n+1) - I(n) \tag{4.1}$$

Second the spatial contrast of each image of the D stack is computed to obtain a differential contrast stack DC. To do so, the local contrast on subregion A of 2x2 px is computed using equation 4.2 where σ is the variance of the pixels in region A. The resulting convoluted image of spatial contrast is the differential contrast on which the propagation of waves is visible.

$$C[A] = \frac{\sigma(D[A])}{mean(I[A])} \tag{4.2}$$

4.3.2. Shear waves velocities retrieval

The waves imaged have frequencies reaching 1kHz. To fulfill Shannon Nyquist theorem the imaging system needs to have a sampling frequency of at least 2kHz. But the CMOS camera can only reach 112Hz of sampling frequency. To overcome this issue, methods compatible with undersampled data are used: time of flight measurement on stromboscopic data and noise correlations. Time of flight is the gold standard to measure wave velocities. It will be used to provide comparisons values with noise correlation.

Time of flight method on stromboscopic data

The CMOS camera is set at its maximum sampling frequency $f_s = 112Hz$. Exposure time is set to 200 μs. The piezo actuator is set to send plane waves at frequency $f_p = nf_s + \delta f$, where n is an integer and $\delta f << f_s$. Between two successive frames, the wave brows $D = n\lambda + \delta d$. This propagation of δd in time T_s gives an apparent velocity c_{app} defined in equation 4.3. The real velocity of the waves is c_{real} defined in equation 4.4. Defining x as $x = \frac{f_s}{f_p}$ from equation 4.4, can be obtained: $c_{\text{real}} = \frac{n\lambda+\delta}{xf_p}$. Noticing that $c_{\text{real}} = \lambda * f_p$ the final equation can be obtained 4.5, allowing to retrieve true celerity from the apparent one.

$$c_{\text{app}} = \delta d * f_s \tag{4.3}$$

$$c_{\text{real}} = D * f_s \tag{4.4}$$

$$c_{\text{real}} = (1 - \frac{n}{x})c_{\text{app}} \tag{4.5}$$

Noise correlation method

Process:
First the temporal correlation for $\tau = 0s$ is computed on every point of the field of view, then the mean is taken. From mean temporal correlation, velocities in the sample are retrieved using equation 1.23.

4.4. Experimental results

4.4.1. Time of flight

In this section time of flight method on stromboscopic data is used to retrieve shear waves velocity. Only one piezoelectric buzzer is placed outside the field of view and is driven to send continuously a sinusoidal wave at a given frequency.

Sample with different elasticities

4 samples are performed with different concentrations of agarose. The more agarose in the sample, the stiffer it gets. The 4 samples are put aside in the field of view. The speckle contrast C defined in equation 3.7 is computed for all the acquisition stack (2000 images). Video of the computed contrast are displayed in the video 4.1 of the link `https://polimi365-my.sharepoint.com/:p:/g/personal/10783888_polimi_it/EQ-mnaP0YCFBgCwLRT5-Wr8BEGwXd9uc9wZnKMAtIxKlxA?e=CD9cXl`. Waves are propagating in the samples and this propagation is visible on the speckle contrast. In particular three consecutives frames are displayed on image 4.6. The time of flight measurement is made by following a wave front (white arrows) on consecutive frames.

Figure 4.4 displays the location of the different elasticities samples in the field of view. The different wavelength according to the stiffness are clearly different. The stiffer the sample, the larger the wavelength gets. Indeed, the stiffer the tissue , the higher is the velocity of shear waves ($E = 3\rho c^2$). For a given frequency, the higher the velocity of shear waves, the larger the wavelength ($c = \lambda\mu$).

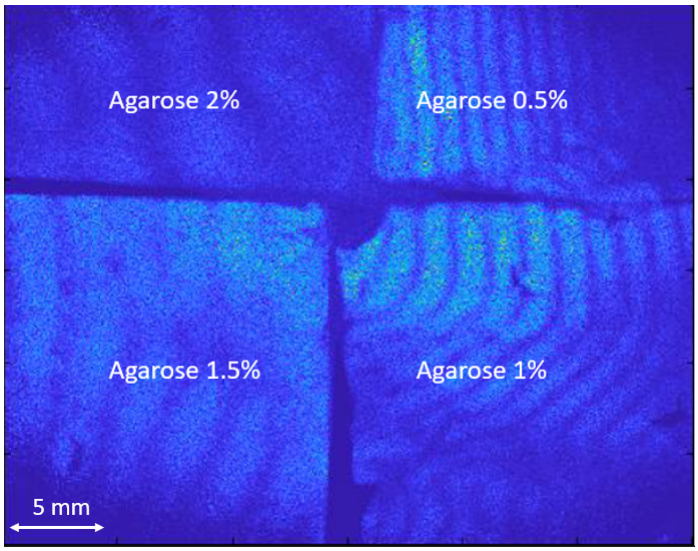

Figure 4.4: Processed image of the contrast of speckle pattern superposed to mass percentage of agarose in the different region of the field of view

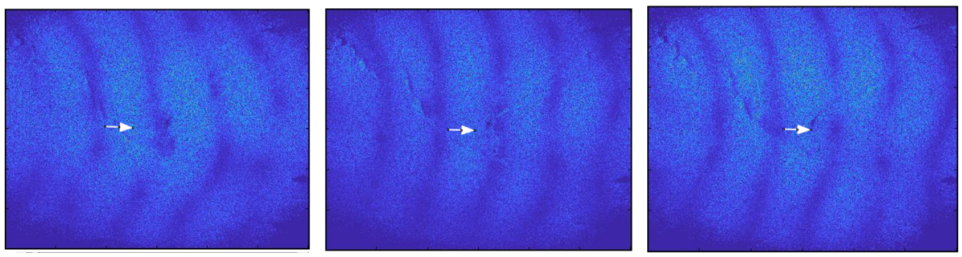

Figure 4.5: Shear waves propagation in sample with 1% agarose, illustration of the time of flight method, arrows indicate the wave front apparent propagation

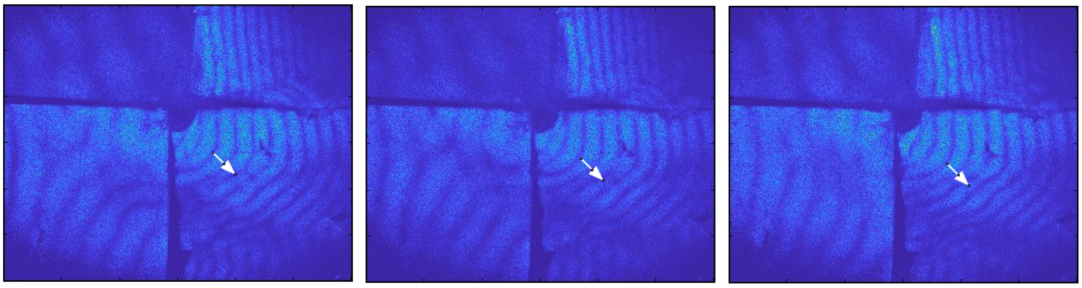

Figure 4.6: Shear waves propagation in 4 different sample with 0.5,1,1.5,2 % agarose mass concentration, illustration of the time of flight method, arrow indicate the wave front apparent propagation, the 4 samples are image simultaneously

Results are displayed in the following table. Velocities and stiffness are found with good agreement with litteracy [40]. The velocities will be used as comparators with the noise

correlation method.

Percentage of agarose (%)	0.5	1	1.5	2
Velocity of shear waves (m/s)	3	6	8	11
Stiffness (kPa)	9	18	24	33

4.4.2. Noise correlation

In this section noise correlation method is used to retrieve shear waves velocity. Shear waves are send through 8 piezoelectric buzzers placed in fixed position all around the field of view and driven by an arduino board to send a sinusoidal wave at a given frequency. When plotting correlation of the field for $\tau = 0s$, the noise signals are filtered out by the correlation process except for the autocorrelation point (central point). This point is therefore set to 0.

Isotropic samples

In this section, homogenous, isotropic sample of given percentage of agarose are studied with an isotropic distribution of the diffuse field. The obtained field is retrieved by computation of the differential spatial contrast in time. The video 5.1 of the previous link displays the acquired field, on which one can qualitatively follow the isotropic propagation of waves front.

The correlation of the field for $\tau = 0s$ is computed and displayed in figure 4.7. Qualitatively the shape of the focal spot is circular, as expected. From this correlation, velocities of 1 m/s for 1% agarose are retrieved by noise correlation .

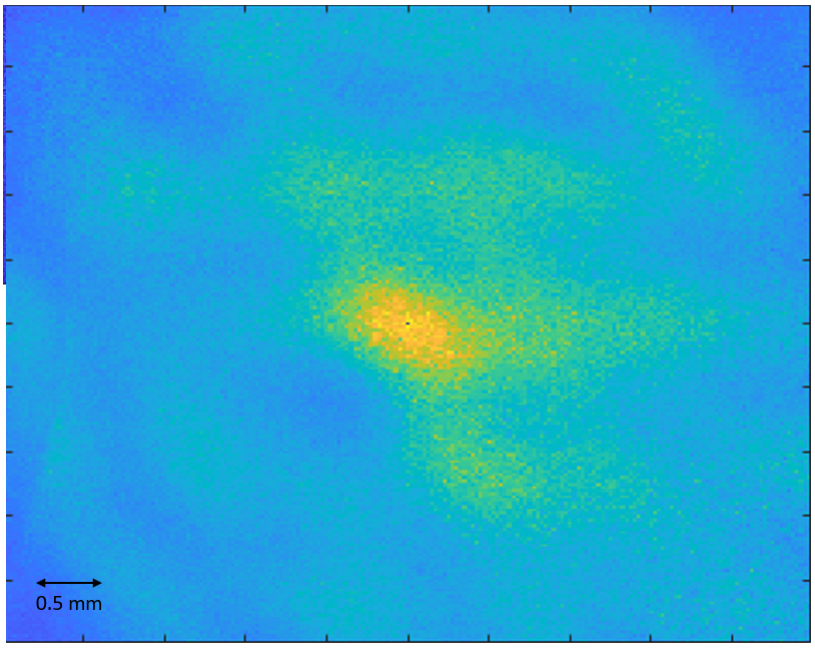

Figure 4.7: Correlation of the diffuse field for $\tau = 0s$ in an isotropic agarose sample (1% agarose, 1% TiO2) with isotropic distribution of the diffuse field around the field of view.

Anisotropic samples

In this section the samples are anisotropic and are studied with an isotropic distribution of the diffuse field. The samples exhibit different velocities according to their propagation direction with respect to the sewing wire embbeded in the agarose matrix.

To test the different directions, two experiments are conducted for each sample. A first experiment is done with an isotropic distribution, if the excitation sources, then the sample is turned of 90° degrees and the same acquisition is obtained with the same locations sources.
The obtain fields, these are retrieved by computation of the differential spatial contrast in time. The video 6.1 and 6.2 of the previous link display the obtained fields. Qualitatively the waves front seems to travel up and down in video 6.1 and side to side in video 6.2. Those observations are in good agreement with an anisotropic sample rotated between the two videos.

Correlation of the obtained fields are computed and displayed in figures 4.8 and 4.9. Looking at the two correlations, one expect to obtain the same spot with a circular rotation of 90°. Qualitatively, focal spot in figure 4.9 is much larger than in figure 4.8. Nevertheless one can notice that the larger dimension happens when the focal spot is

rotated 90°. Waves velocities retrieval are around 1 m/s with an anisotropic ratio around 1/2.

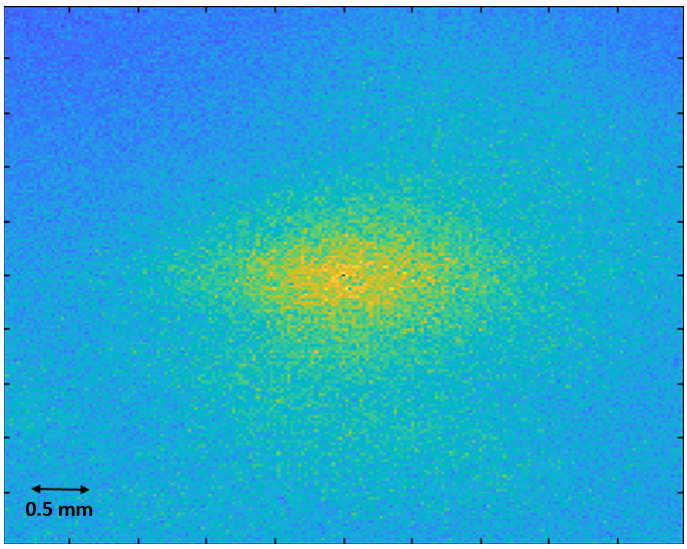

Figure 4.8: Correlation of the diffuse field for $\tau = 0s$ in an anisotropic agarose sample (1% agarose, 1% TiO2, sewing wire), with isotropic distribution of the diffuse field around the field of view.

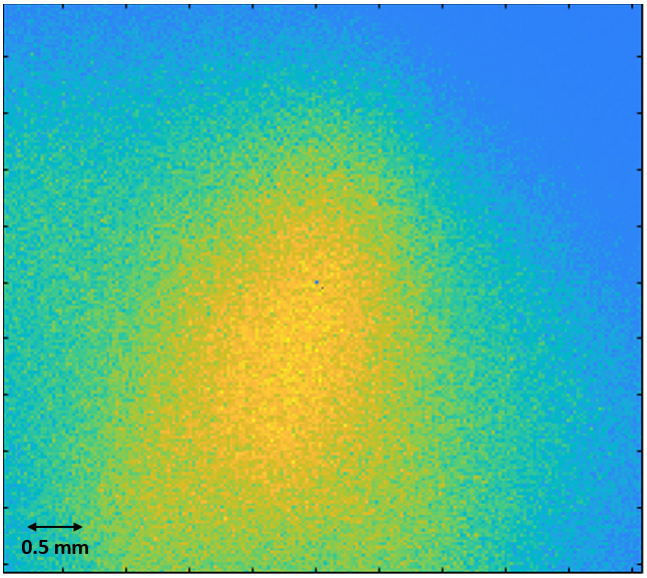

Figure 4.9: Correlation of the diffuse field for $\tau = 0s$ in an anisotropic agarose sample (1% agarose, 1% TiO2, sewing wire), with isotropic distribution of the diffuse field around the field of view, the sample has been rotated of 90° with respect to figure 4.8

Anisotropic distribution of the piezo buzzers

In this section samples with constant stiffness are studied with anisotropic distributions of piezoelectric buzzers. The buzzers are only placed on the low half of the sample, outside the field of view. The obtained field is retrieved by computation of the differential spatial contrast in time. The video 5.2 of the previous link displays the obtained field, on which one can qualitatively follow the anisotropic propagation of wave fronts travelling from the bottom to the top of the field of view.

Correlation of the retrieved wave field is computed for $\tau = 0s$ and displayed in figure 4.10. The shape of the focal spot is elliptic, there is a biais in velocity retrieval.

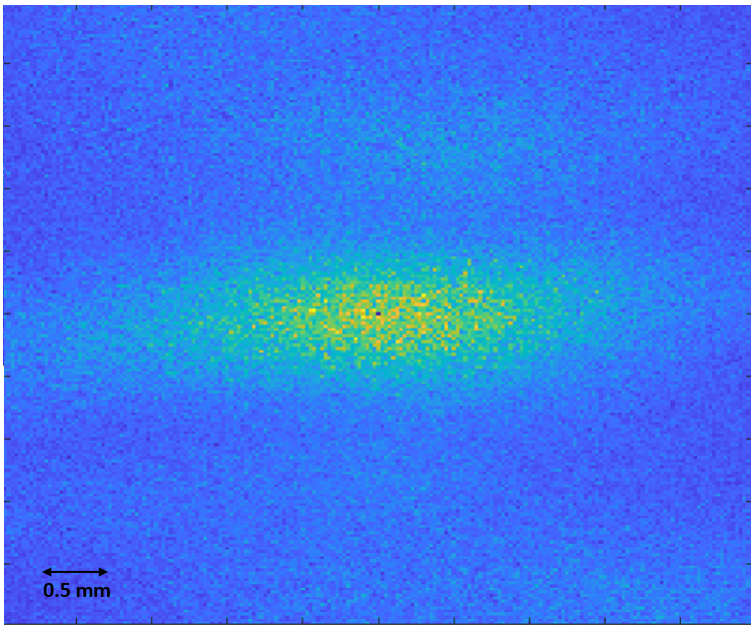

Figure 4.10: Correlation of the diffuse field for $\tau = 0s$ in an isotropic agarose sample (1% agarose, 1% TiO2) with anisotropic distribution of the diffuse field around the field of view.

4.5. Discussions

The results presented above are preliminary.
Summary of workflow of the experiments presented in introduction:

1. Verify the ability of Laser Speckle Imaging to retrieve with good result elasticity of Agarose samples using the gold standard method of time of flight. Mechanically isotropic and anisotropic agarose samples will be characterized.

2. Retrieve elasticity of agarose samples using correlation of a diffuse field method, taking as comparison the gold standard method.
3. Underline experimentally the bias in the measured velocities of waves with anisotropic distribution of the diffuse field sources.
4. Show that the previous situation can be detected and then avoid to follow the former proposed decision tree.

Step 1) was successfully implemented and has proven the ability of Laser Speckle imaging to perform elastography on soft tissues. A further development could be to apply this method to anisotropic samples to provide comparison value with noise correlation method.

Step 2) was successfully implemented and noise correlation method was proven to work on isotropic sample. Further developments will be first to conduct a repeatability study on the retrieve values, second, to perform a proper comparison with the gold standard method on isotropic and anisotropic samples of different elasticities.

Step 3) was successfully implemented, the bias in measured velocities was highlited in case of anisotropic distribution of excitation sources around the field of view.

Step 4) is still under work. To apply the proposed algorithm, one need to compute the diffuses field correlation during propagation, for τ different to 0.

5 | Conclusions and futur developments

5.1. Main conclusions

Mechanical anisotropy of biological tissues is a way to characterized matter and can be linked to several pathologies [9, 25, 29].
Noise correlation method combined with optical elastography allows for uncontact retrieval of viscoelastic properties of matter [30, 40].
In this work, a bias in mechanical anisotropy of matter retrieval by noise correlation is highlighted. Simulation of elastic waves propagation in 2D medium were implemented. A classifier algorithm able to target the situations leading to errors is proposed based on the simulations. Experimental verifications on agarose samples presenting isotropic and anisotropic mechanical properties are performed. Laser speckle imaging is used and prooved to provide good results for elastography with the gold standard method of time of flight on stromboscopic data. Laser speckle imaging elastography is then performed on agarose samples with noise correlation method. Preliminary results show good agreement with the gold standard method. Using noise correlation method, a bias in the retrieval of anisotropy of tissue is highlited experimentally.

5.2. Main axes of research

5.2.1. Improvement of the method

Anisotropy retrieval in any cases

The proposed decision tree is a detection tool of a situation leading to errors in the measurement of mechanical anisotropy. One development of this thesis is not only to detect the error's situation but to quantify the error and to provide a correction factor.

Let's do an analogy with optic. Let's take a monochromatic point source emitting a beam passing through a objective (see figure 5.1).

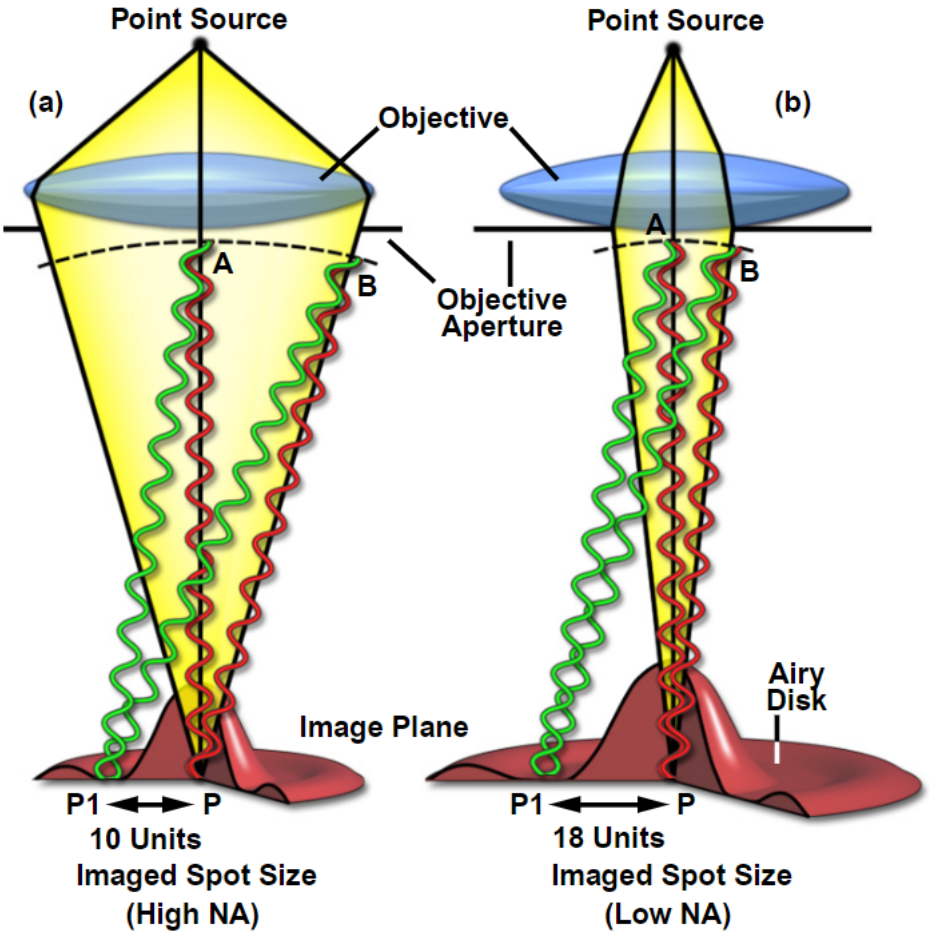

Figure 5.1: Diffraction and Airy spot [2]

The image of the source observed on the screen is no longer a point due to the diffraction phenomenon. The obtained spot is called the focal spot, point spread function or Airy spot.

Its dimensions were derived by Ernst Abbe in its groundmaking work [59]. The lateral dimensions $r_{x,y}$ follow equation 5.1 with λ the wavelength of light and NA the numerical aperture of the objective. The highest the numerical aperture, the shorter is the spot size, the more resolute is the optical set-up.

$$r_{x,y} = \frac{\lambda}{2NA} \tag{5.1}$$

The spot is actually a bean with an axial extension r_z that follows equation 5.2. Again,

parameters are λ the wavelength of light and NA the numerical aperture of the objective.

$$r_z = \frac{2\lambda}{NA^2} \tag{5.2}$$

In our case, waves are not electromagnetic but acoustic waves, and the field is diffuse. We have seen that the causal part of correlation of a diffuse field is equivalent to the propagation of an impulse in the media. The correlation at $\tau = 0s$ can be seen as the impulse response of the field. As for the Airy spot in optics, one could correlate the dimension of the impulse response of the field with the parameters of the diffraction process. In particular one could define the aperture of the refocusing process. By defining an aperture of the diffuse field, one could quantify the anisotropy of the diffuse field distribution using the shape of the correlation at $\tau = 0s$. Once the numerical aperture of the field is known, one can retrieve the velocity of shear waves with a correcting factor due to the numerical aperture of the field.

Study on viscous anisotropic properties in samples

Until now we considered the samples as fully elastic. Viscous properties of matter were discarded in simulations and in experimental samples. One axis of research will be not only to characterized anisotropy of matter by its shear elastic modulus in different directions but also with its shear viscosity modulus in different directions.

5.2.2. Application to biological tissues

This specific work's aims at showing that one can retrieve mechanical properties in anisotropic samples by noise correlation method without any bias in the measurement. In a broader scope, it aims at biological applications, in particular retrieving anisotropic properties of biological tissues in vivo.

In this scope, next step will be the characterization of biological sample ex-vivo. Straighfoward candidate will be muscle tissue because of its large availabilities. However, liver, skin, cornea, brain tissues are under scrutiny.

In this scope, one could consider to review former study made on anisotropic samples under the asumption of isotropic mechanical properties and perform a refinement of the output properties holding anisotropy into account. One example is the study of pork liver performed by A. Marmin in the iCube laboratory where this thesis is conducted. Results presented in figure 5.2 were obtained by digital holography under the hypothesis of an isotropic distribution of excitation sources and a isotropic tissues.

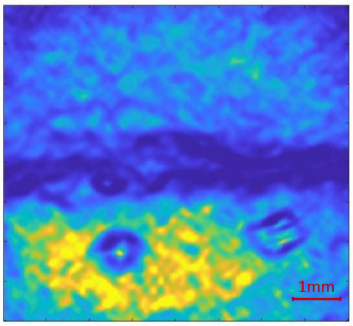

Figure 5.2: Pork liver elasticity map (a.u) retrieved using noise correlation. The upper side was raw and the other side was cooked, taken from [40]

5.2.3. In vivo application to anisotropic tissues

Once the technique is proven to work ex vivo on biological samples, characterization of in vivo tissues could be considered.

Laser Speckle set-up could be embbeded in a multi modal plateform used in open surgery. In the iCube laboratory, diffuse optic is under study. It provides real-time, wide-field and high-quality single snapshot imaging of optical properties of matter [8, 58]. To retrieve in real time optical absorption and scattering coefficients of matter it uses Lasers. Laser imaging signals could be used to retrieve mechanical properties of matter.
In particular, a multispectral plateform has been developped to fit for open surgery. It is displayed in figure 5.3. The coupling of this device with the noise correlation method could allow to perform in vivo, real time measure of viscoelastic properties of matter in a surgical theater.

Not only open surgery is at stake. The possibility to embedded Laser Speckle Imaging in an endoscope for colorectal cancer screening could be major breakthrough in colonoscopy. As described in figure 5.4, a colonoscope is a flexible tube able to image the wall of the colon of the patient. In case of cancer, the patient can present polype that can be removed during colonoscopy. Risk of failure of the operation rises when the removal of polype is uncomplete. By adding a Laser at the top of the colonoscope, Laser speckle imaging could help to distinguish healthy from tumerous tissues. Laser speckle imaging is a good candidate for elastography of the colon.

Coupled with the noise correlation method, Laser speckle imaging is a non contact, real-time that could be a powerful tool for helping to distinguish healthy from pathologious tissues.

Figure 5.3: Multispectral optical imaging in real-time for surgery devellopped in the iCube laboratory by S. Segaud

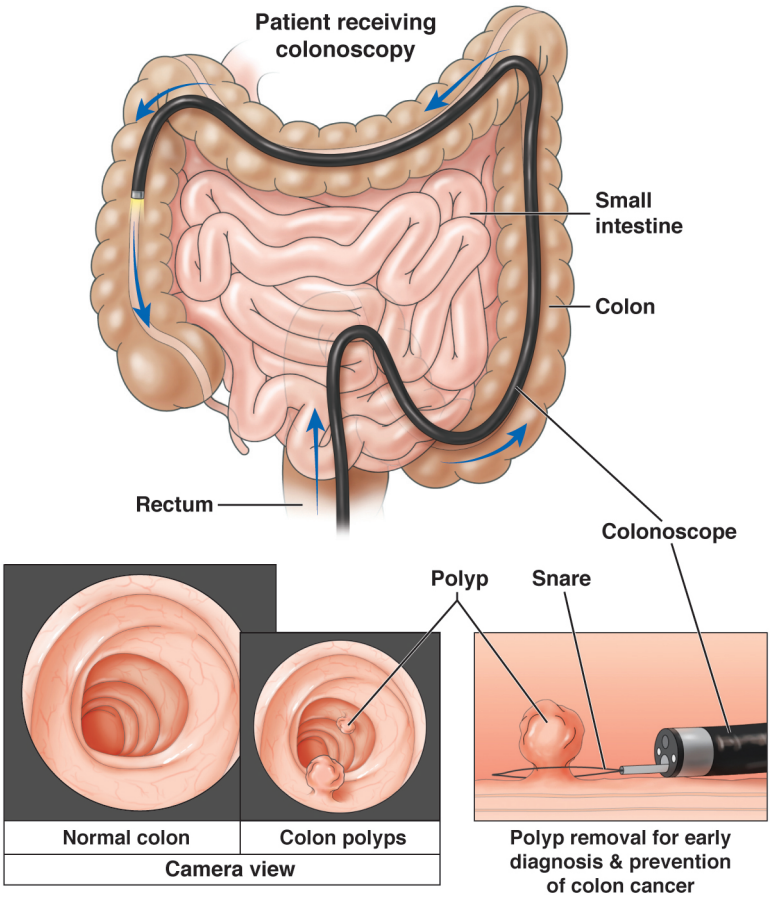

Figure 5.4: Coloscopy procedure, taken from [21]

Bibliography

[1] bmjopen-2016-January-6-1–F2.large.jpg (JPEG Image, 1280 × 729 pixels), . URL https://bmjopen.bmj.com/content/bmjopen/6/1/e008848/F2.large.jpg.

[2] The Diffraction Barrier in Optical Microscopy, . URL https://www.microscopyu.com/techniques/super-resolution/the-diffraction-barrier-in-optical-microscopy.

[3] Edge Detection in Ultrasonic Speckle, . URL http://www.brl.uiuc.edu/Projects/edge_detection_in_ultrasonic_speckle.php.

[4] Laser Speckle and Applications in Optics - 1st Edition, . URL https://www.elsevier.com/books/laser-speckle-and-applications-in-optics/francon/978-0-12-265760-3.

[5] The Online Marketplace with Weekly Auctions, . URL https://www.catawiki.com/en/.

[6] Ultrafast imaging of cell elasticity with optical microelastography | PNAS, . URL https://www.pnas.org/doi/10.1073/pnas.1713395115.

[7] Muscle - Definition, Function, Types and Structure, Dec. 2017. URL https://biologydictionary.net/muscle/.

[8] E. Aguénounon, J. T. Smith, M. Al-Taher, M. Diana, X. Intes, and S. Gioux. Real-time, wide-field and high-quality single snapshot imaging of optical properties with profile correction using deep learning. *Biomedical Optics Express*, 11(10):5701–5716, Sept. 2020. ISSN 2156-7085. doi: 10.1364/BOE.397681. URL https://www.ncbi.nlm.nih.gov/pmc/articles/PMC7587245/.

[9] A. L. Alexander, J. E. Lee, M. Lazar, and A. S. Field. Diffusion tensor imaging of the brain. *DIFFUSION TENSOR IMAGING*, 4(3):14, 2007.

[10] J. P. Allen and M. M. o. A. N. Y. N.Y.). *The Art of Medicine in Ancient Egypt*. Metropolitan Museum of Art, 2005. ISBN 978-1-58839-170-4. Google-Books-ID: jNbVl5LOjHUC.

[11] B. A. Auld. Rayleigh Wave Propagation. In E. A. Ash and E. G. S. Paige, editors, *Rayleigh-Wave Theory and Application*, Springer Series on Wave Phenomena, pages 12–28, Berlin, Heidelberg, 1985. Springer. ISBN 978-3-642-82621-4. doi: 10.1007/978-3-642-82621-4_2.

[12] D. A. Boas and A. K. Dunn. Laser speckle contrast imaging in biomedical optics. *Journal of Biomedical Optics*, 15(1):011109, 2010. ISSN 10833668. doi: 10.1117/1.3285504. URL http://biomedicaloptics.spiedigitallibrary.org/article.aspx?doi=10.1117/1.3285504.

[13] S. Catheline, J.-L. Gennisson, G. Delon, M. Fink, R. Sinkus, S. Abouelkaram, and J. Culioli. Measurement of viscoelastic properties of homogeneous soft solid using transient elastography: An inverse problem approach. *The Journal of the Acoustical Society of America*, 116(6):3734–3741, Dec. 2004. ISSN 0001-4966. doi: 10.1121/1.1815075. URL https://asa.scitation.org/doi/10.1121/1.1815075. Publisher: Acoustical Society of America.

[14] S. Catheline, R. Souchon, M. Rupin, J. Brum, A. H. Dinh, and J.-Y. Chapelon. Tomography from diffuse waves: Passive shear wave imaging using low frame rate scanners. *Applied Physics Letters*, 103(1):014101, July 2013. ISSN 0003-6951. doi: 10.1063/1.4812515. URL https://aip.scitation.org/doi/10.1063/1.4812515. Publisher: American Institute of Physics.

[15] S. Catheline, R. Souchon, M. Rupin, J. Brum, A. H. Dinh, and J.-Y. Chapelon. Tomography from diffuse waves: Passive shear wave imaging using low frame rate scanners. *Applied Physics Letters*, 103(1):014101, July 2013. ISSN 0003-6951, 1077-3118. doi: 10.1063/1.4812515. URL http://aip.scitation.org/doi/10.1063/1.4812515.

[16] X. Chen, Y. Wang, J. Lu, and P. Li. Simultaneous viscosity and elasticity measurement using laser speckle contrast imaging. *Optics Letters*, 43(7):1582, Apr. 2018. ISSN 0146-9592, 1539-4794. doi: 10.1364/OL.43.001582. URL https://opg.optica.org/abstract.cfm?URI=ol-43-7-1582.

[17] G. Cloutier, F. Destrempes, F. Yu, and A. Tang. Quantitative ultrasound imaging of soft biological tissues: a primer for radiologists and medical physicists. *Insights into Imaging*, 12, Dec. 2021. doi: 10.1186/s13244-021-01071-w.

[18] M. M. Doyley and K. J. Parker. Elastography. *Ultrasound Clinics*, 9(1):1–11, Jan. 2014. ISSN 1556858X. doi: 10.1016/j.cult.2013.09.006. URL https://linkinghub.elsevier.com/retrieve/pii/S1556858X13001060.

[19] M. M. Doyley and K. J. Parker. Elastography: general principles and clincial applications. *Ultrasound Clinics*, 9(1):1–11, Jan. 2014. ISSN 1556-858X. doi: 10.1016/j.cult.2013.09.006.

[20] A. K. Dunn, A. Devor, H. Bolay, M. L. Andermann, M. A. Moskowitz, A. M. Dale, and D. A. Boas. Simultaneous imaging of total cerebral hemoglobin concentration, oxygenation, and blood flow during functional activation. *Optics Letters*, 28(1):28–30, Jan. 2003. ISSN 1539-4794. doi: 10.1364/OL.28.000028. URL `https://opg.optica.org/ol/abstract.cfm?uri=ol-28-1-28`. Publisher: Optica Publishing Group.

[21] J. E. East. Can Colonoscopy Sow the Seeds of Colorectal Cancer? *Gastroenterology*, 157(5):1192–1195, Nov. 2019. ISSN 0016-5085, 1528-0012. doi: 10.1053/j.gastro.2019.09.004. URL `https://www.gastrojournal.org/article/S0016-5085%2819%2941335-8/fulltext#relatedArticles`. Publisher: Elsevier.

[22] M. Fink. From Loschmidt daemons to time-reversed waves. *Philosophical Transactions of the Royal Society A: Mathematical, Physical and Engineering Sciences*, 374: 20150156, June 2016. doi: 10.1098/rsta.2015.0156.

[23] T. Gallot, S. Catheline, P. Roux, J. Brum, N. Benech, and C. Negreira. Passive elastography: shear-wave tomography from physiological-noise correlation in soft tissues. *IEEE transactions on ultrasonics, ferroelectrics, and frequency control*, 58 (6):1122–1126, June 2011. ISSN 1525-8955. doi: 10.1109/TUFFC.2011.1920.

[24] B. S. Garra. Elastography: history, principles, and technique comparison. *Abdominal Imaging*, 40(4):680–697, Apr. 2015. ISSN 1432-0509. doi: 10.1007/s00261-014-0305-8. URL `https://doi.org/10.1007/s00261-014-0305-8`.

[25] J.-L. Gennisson, S. Catheline, S. Chaffaı, and M. Fink. Transient elastography in anisotropic medium: Application to the measurement of slow and fast shear wave speeds in muscles. *The Journal of the Acoustical Society of America*, 114(1):536–541, July 2003. ISSN 0001-4966. doi: 10.1121/1.1579008. URL `http://asa.scitation.org/doi/10.1121/1.1579008`.

[26] J.-L. Gennisson, T. Deffieux, E. Macé, G. Montaldo, M. Fink, and M. Tanter. Viscoelastic and Anisotropic Mechanical Properties of in vivo Muscle Tissue Assessed by Supersonic Shear Imaging. *Ultrasound in Medicine & Biology*, 36(5):789–801, May 2010. ISSN 0301-5629. doi: 10.1016/j.ultrasmedbio.2010.02.013. URL `https://www.sciencedirect.com/science/article/pii/S0301562910000761`.

[27] J. L. Gennisson, T. Deffieux, M. Fink, and M. Tanter. Ultrasound elastography: Principles and techniques. *Diagnostic and Interventional Imaging*, 94(5):487–495,

May 2013. ISSN 2211-5684. doi: 10.1016/j.diii.2013.01.022. URL https://www.sciencedirect.com/science/article/pii/S2211568413000302.

[28] J. W. Goodman. *Speckle Phenomena in Optics: Theory and Applications, Second Edition*. SPIE, Jan. 2020. ISBN 978-1-5106-3149-6. doi: 10.1117/3.2548484. URL https://www.spiedigitallibrary.org/ebooks/PM/Speckle-Phenomena-in-Optics-Theory-and-Applications-Second-Edition/eISBN-9781510631496/10.1117/3.2548484.

[29] P. Kalra, B. Raterman, X. Mo, and A. Kolipaka. Magnetic resonance elastography of brain: Comparison between anisotropic and isotropic stiffness and its correlation to age. *Magnetic Resonance in Medicine*, 82(2):671–679, Aug. 2019. ISSN 1522-2594. doi: 10.1002/mrm.27757.

[30] B. F. Kennedy, P. Wijesinghe, and D. D. Sampson. The emergence of optical elastography in biomedicine. *Nature Photonics*, 11(4):215–221, Apr. 2017. ISSN 1749-4885, 1749-4893. doi: 10.1038/nphoton.2017.6. URL http://www.nature.com/articles/nphoton.2017.6.

[31] N. H. Koshoji, S. K. Bussadori, C. C. Bortoletto, M. T. Oliveira, R. A. Prates, and A. M. Deana. Analysis of eroded bovine teeth through laser speckle imaging. In *Lasers in Dentistry XXI*, volume 9306, pages 59–64. SPIE, Feb. 2015. doi: 10.1117/12.2075195. URL https://www.spiedigitallibrary.org/conference-proceedings-of-spie/9306/93060D/Analysis-of-eroded-bovine-teeth-through-laser-speckle-imaging/10.1117/12.2075195.full.

[32] T. A. Krouskop. A pulsed Doppler ultrasonic system for making noninvasive measurements of the mechanical properties of soft tissue. page 8, 1987.

[33] T. A. Krouskop. A pulsed Doppler ultrasonic system for making noninvasive measurements of the mechanical properties of soft tissue. page 8, 1987.

[34] G. Laloy-Borgna, A. Zorgani, and S. Catheline. Micro-elastography: Toward ultrasonic shear waves in soft solids. *Applied Physics Letters*, 118(11):113701, Mar. 2021. ISSN 0003-6951, 1077-3118. doi: 10.1063/5.0039816. URL https://aip.scitation.org/doi/10.1063/5.0039816.

[35] Larose, L. Margerin, A. Derode, B. Van Tiggelen, N. Shapiro, A. Paul, M. Campillo, L. Stehly, and M. Tanter. Correlation of random wavefields: An interdisciplinary review. *Geophysics*, 71(4):SI11–SI21, 2006. doi: 10.1190/1.2213356. URL https:

//hal-insu.archives-ouvertes.fr/insu-00267103. Publisher: Society of Exploration Geophysicists.

[36] X. Leng, R. Japaer, H. Zhang, M. Yeerlan, F. Ma, and J. Ding. Relationship of shear wave elastography anisotropy with tumor stem cells and epithelial-mesenchymal transition in breast cancer. *BMC Medical Imaging*, 21(1):171, Nov. 2021. ISSN 1471-2342. doi: 10.1186/s12880-021-00707-z. URL https://doi.org/10.1186/s12880-021-00707-z.

[37] S. S. Leong, J. H. D. Wong, M. N. Md Shah, A. Vijayananthan, M. Jalalonmuhali, N. H. Mohd Sharif, N. K. Abas, and K. H. Ng. Stiffness and Anisotropy Effect on Shear Wave Elastography: A Phantom and in Vivo Renal Study. *Ultrasound in Medicine & Biology*, 46(1):34–45, Jan. 2020. ISSN 1879-291X. doi: 10.1016/j.ultrasmedbio.2019.08.011.

[38] W. T. H. Lim, E. H. Ooi, J. J. Foo, K. H. Ng, J. H. D. Wong, and S. S. Leong. Shear Wave Elastography: A Review on the Confounding Factors and Their Potential Mitigation in Detecting Chronic Kidney Disease. *Ultrasound in Medicine & Biology*, 47(8):2033–2047, Aug. 2021. ISSN 0301-5629. doi: 10.1016/j.ultrasmedbio.2021.03.030. URL https://www.sciencedirect.com/science/article/pii/S0301562921001514.

[39] Y. K. Mariappan, K. J. Glaser, and R. L. Ehman. Magnetic resonance elastography: A review. *Clinical Anatomy*, 23(5):497–511, 2010. ISSN 1098-2353. doi: 10.1002/ca.21006. URL https://onlinelibrary.wiley.com/doi/abs/10.1002/ca.21006. _eprint: https://onlinelibrary.wiley.com/doi/pdf/10.1002/ca.21006.

[40] A. Marmin, S. Catheline, and A. Nahas. Full-field passive elastography using digital holography. *Optics Letters*, 45(11):2965, June 2020. ISSN 0146-9592, 1539-4794. doi: 10.1364/OL.388327. URL https://opg.optica.org/abstract.cfm?URI=ol-45-11-2965.

[41] A. Marmin, G. Laloy-Borgna, S. Facca, S. Gioux, S. Catheline, and A. Nahas. Time-of-flight and noise-correlation-inspired algorithms for full-field shear-wave elastography using digital holography. *Journal of Biomedical Optics*, 26(8):086006, Aug. 2021. ISSN 1083-3668, 1560-2281. doi: 10.1117/1.JBO.26.8.086006. URL https://www.spiedigitallibrary.org/journals/journal-of-biomedical-optics/volume-26/issue-8/086006/Time-of-flight-and-noise-correlation-inspired-algorithms-for-full/10.1117/1.JBO.26.8.086006.full. Publisher: SPIE.

[42] I. Z. Nenadic, B. Qiang, M. W. Urban, H. Zhao, W. Sanchez, J. F. Greenleaf, and S. Chen. Attenuation measuring ultrasound shearwave elastography and *in vivo* application in post-transplant liver patients. *Physics in Medicine and Biology*, 62 (2):484–500, Jan. 2017. ISSN 0031-9155, 1361-6560. doi: 10.1088/1361-6560/aa4f6f. URL https://iopscience.iop.org/article/10.1088/1361-6560/aa4f6f.

[43] R. Pandiselvam, V. P. Mayookha, A. Kothakota, S. V. Ramesh, R. Thirumdas, and P. Juvvi. Biospeckle laser technique – A novel non-destructive approach for food quality and safety detection. *Trends in Food Science & Technology*, 97:1–13, Mar. 2020. ISSN 0924-2244. doi: 10.1016/j.tifs.2019.12.028. URL https://www.sciencedirect.com/science/article/pii/S0924224419304625.

[44] S. Papazoglou, J. Braun, U. Hamhaber, and I. Sack. Two-dimensional waveform analysis in MR elastography of skeletal muscles. *Physics in Medicine and Biology*, 50(6):1313–1325, Mar. 2005. ISSN 0031-9155, 1361-6560. doi: 10.1088/0031-9155/50/6/018. URL https://iopscience.iop.org/article/10.1088/0031-9155/50/6/018.

[45] E. C. Qin, R. Sinkus, G. Geng, S. Cheng, M. Green, C. D. Rae, and L. E. Bilston. Combining MR elastography and diffusion tensor imaging for the assessment of anisotropic mechanical properties: A phantom study. *Journal of Magnetic Resonance Imaging*, 37(1):217–226, 2013. ISSN 1522-2586. doi: 10.1002/jmri.23797. URL https://onlinelibrary.wiley.com/doi/abs/10.1002/jmri.23797. _eprint: https://onlinelibrary.wiley.com/doi/pdf/10.1002/jmri.23797.

[46] E. C. Qin, L. Jugé, S. A. Lambert, V. Paradis, R. Sinkus, and L. E. Bilston. In Vivo Anisotropic Mechanical Properties of Dystrophic Skeletal Muscles Measured by Anisotropic MR Elastographic Imaging: The mdx Mouse Model of Muscular Dystrophy. *Radiology*, 273(3):726–735, Dec. 2014. ISSN 0033-8419, 1527-1315. doi: 10.1148/radiol.14132661. URL http://pubs.rsna.org/doi/10.1148/radiol.14132661.

[47] E. C. Qin, L. Jugé, S. A. Lambert, V. Paradis, R. Sinkus, and L. E. Bilston. In Vivo Anisotropic Mechanical Properties of Dystrophic Skeletal Muscles Measured by Anisotropic MR Elastographic Imaging: The mdx Mouse Model of Muscular Dystrophy. *Radiology*, 273(3):726–735, Dec. 2014. ISSN 0033-8419, 1527-1315. doi: 10.1148/radiol.14132661. URL http://pubs.rsna.org/doi/10.1148/radiol.14132661.

[48] H. Rabal and R. Braga. *Dynamic Laser Speckle and Applications*. Jan. 2008. ISBN 978-1-4200-6015-7. doi: 10.1201/9781420060164. Journal Abbreviation: Dynamic

Laser Speckle and Applications Publication Title: Dynamic Laser Speckle and Applications.

[49] N. C. Rouze, M. H. Wang, M. L. Palmeri, and K. R. Nightingale. Finite element modeling of impulsive excitation and shear wave propagation in an incompressible, transversely isotropic medium. *Journal of Biomechanics*, 46(16):2761–2768, Nov. 2013. ISSN 0021-9290. doi: 10.1016/j.jbiomech.2013.09.008. URL https://www.sciencedirect.com/science/article/pii/S0021929013004193.

[50] D. ROYER and E. Dieulesaint. *Elastic Waves in Solids I: Free and Guided Propagation*. Springer Science & Business Media, Nov. 1999. ISBN 978-3-540-65932-7. Google-Books-ID: 1sHbvgEACAAJ.

[51] D. Royer and T. Valier-Brasier. *Elastic Waves in Solids 1: Propagation*. Wiley, 1 edition, Mar. 2022. ISBN 978-1-78630-814-6 978-1-119-90294-2. doi: 10.1002/9781119902942. URL https://onlinelibrary.wiley.com/doi/book/10.1002/9781119902942.

[52] O. V. Rudenko and A. P. Sarvazyan. Wave anisotropy of shear viscosity and elasticity. *Acoustical Physics*, 60(6):710–718, Nov. 2014. ISSN 1063-7710, 1562-6865. doi: 10.1134/S1063771014060141. URL http://link.springer.com/10.1134/S1063771014060141.

[53] A. P. Sarvazyan, M. W. Urban, and J. F. Greenleaf. Acoustic Waves in Medical Imaging and Diagnostics. *Ultrasound in Medicine & Biology*, 39(7):1133–1146, July 2013. ISSN 0301-5629. doi: 10.1016/j.ultrasmedbio.2013.02.006. URL https://www.sciencedirect.com/science/article/pii/S0301562913000793.

[54] G. Scarcelli, W. J. Polacheck, H. T. Nia, K. Patel, A. J. Grodzinsky, R. D. Kamm, and S. H. Yun. Noncontact three-dimensional mapping of intracellular hydromechanical properties by Brillouin microscopy. *Nature Methods*, 12(12):1132–1134, Dec. 2015. ISSN 1548-7105. doi: 10.1038/nmeth.3616. URL https://www.nature.com/articles/nmeth.3616. Number: 12 Publisher: Nature Publishing Group.

[55] N. M. Shapiro, M. Campillo, L. Stehly, and M. H. Ritzwoller. High-Resolution Surface-Wave Tomography from Ambient Seismic Noise. *Science*, 307(5715):1615–1618, Mar. 2005. ISSN 0036-8075, 1095-9203. doi: 10.1126/science.1108339. URL https://www.science.org/doi/10.1126/science.1108339.

[56] M. Singh, J. Li, Z. Han, C. Wu, S. R. Aglyamov, M. D. Twa, and K. V. Larin. Investigating Elastic Anisotropy of the Porcine Cornea as a Function of Intraocular Pressure With Optical Coherence Elastography. *Journal of refractive*

surgery (Thorofare, N.J. : 1995), 32(8):562–567, Aug. 2016. ISSN 1081-597X. doi: 10.3928/1081597X-20160520-01. URL https://www.ncbi.nlm.nih.gov/pmc/articles/PMC5409833/.

[57] D. J. Tweten, R. J. Okamoto, J. L. Schmidt, J. R. Garbow, and P. V. Bayly. Estimation of material parameters from slow and fast shear waves in an incompressible, transversely isotropic material. *Journal of Biomechanics*, 48(15):4002–4009, Nov. 2015. ISSN 00219290. doi: 10.1016/j.jbiomech.2015.09.009. URL https://linkinghub.elsevier.com/retrieve/pii/S0021929015005035.

[58] J. Vervandier and S. Gioux. Single snapshot imaging of optical properties. *Biomedical Optics Express*, 4(12):2938–2944, 2013. ISSN 2156-7085. doi: 10.1364/BOE.4.002938.

[59] H. Volkmann. Ernst Abbe and His Work. *Applied Optics*, 5(11):1720–1731, Nov. 1966. ISSN 2155-3165. doi: 10.1364/AO.5.001720. URL https://opg.optica.org/ao/abstract.cfm?uri=ao-5-11-1720. Publisher: Optica Publishing Group.

[60] Wei-Ning Lee, M. Pernot, M. Couade, E. Messas, P. Bruneval, A. Bel, A. A. Hagege, M. Fink, and M. Tanter. Mapping Myocardial Fiber Orientation Using Echocardiography-Based Shear Wave Imaging. *IEEE Transactions on Medical Imaging*, 31(3):554–562, Mar. 2012. ISSN 0278-0062, 1558-254X. doi: 10.1109/TMI.2011.2172690. URL http://ieeexplore.ieee.org/document/6054058/.

[61] J. Zizka, A. Olwal, and R. Raskar. SpeckleSense: fast, precise, low-cost and compact motion sensing using laser speckle. In *Proceedings of the 24th annual ACM symposium on User interface software and technology - UIST '11*, page 489, Santa Barbara, California, USA, 2011. ACM Press. ISBN 978-1-4503-0716-1. doi: 10.1145/2047196.2047261. URL http://dl.acm.org/citation.cfm?doid=2047196.2047261.

A | Appendix

A.1. Second approach by time symmetry

This paragraph propose a second approach to detect unbalance partition of source around the reicever point. It has been proven in seismologic field that the Green's function anticausal (t<0) part and causal part (t>0) are symmetric in time with respect to t=0s [55]. For unbalance repartition of source around the receiver, this time symmetry is lost and the wave is coming from the sources direction (t<0s) and propagate in the oposite direction (t>0s).

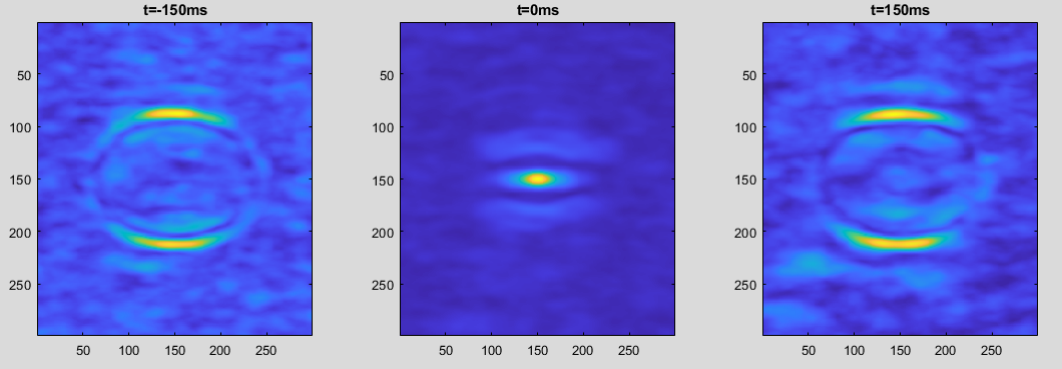

Figure A.1: Decision tree for classification, S the symmetry index is defined in equation 3.6, C the ellipse index is defined in equation 3.7, T1,T2 are arbitrary thresholds

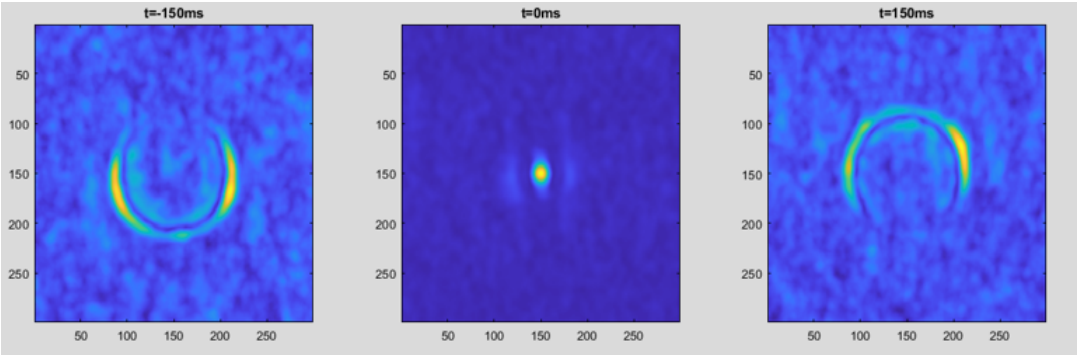

Figure A.2: Decision tree for classification, S the symmetry index is defined in equation 3.6, C the ellipse index is defined in equation 3.7, T1,T2 are arbitrary thresholds

List of Figures

Acknowledgements

Thanks to you, Amir, for this great subject, and for the trust. I personnaly think you are a great manager.
Thanks to Agathe for knowledge transfer, A. Aliverti for the regular checkups, Vittoria for correcting my italian, Ado for mental support and last but not least, thanks to the whole IPP team for its welcoming spirit.